JOURNAL OF GEOPHYSICAL RESEARCH, VOL. 111, C05015, doi:10.1029/2005JC002989, 2006

Correction published 16 March 2007

Intraseasonal variability near 10°N in the eastern tropical Pacific Ocean

J. Thomas Farrar[1] and Robert A. Weller[2]

Received 7 April 2005; revised 6 January 2006; accepted 30 January 2006; published 20 May 2006.

[1] New in situ observations from 10°N, 125°W during 1997–1998 show strong intraseasonal variability in meridional velocity and sea surface temperature. The 50- to 100-day oscillations in sea surface height (SSH) have long been recognized as a prominent aspect of oceanic variability in the region of 9–13°N in the eastern Pacific Ocean. We use in situ and satellite data to more fully characterize this variability. The oscillations have zonal wavelengths of 550–1650 km and propagate westward in a manner consistent with the dispersion relation for first baroclinic mode, free Rossby waves in the presence of a mean westward flow. Analysis of 9 years of altimetry data shows that the amplitude of the 50- to 100-day SSH variability at 10°N is largest on 90–115°W, with peak amplitudes occurring around April. Some eddies traveling westward at 10–13°N emanate from near the gulfs of Tehuantepec and Papagayo, but eddies sometimes also appear to intensify well away from the coast while in the North Equatorial Current (NEC). The hypothesis that the intraseasonal variability and its annual cycle are associated with baroclinic instability of the NEC is supported by a spatiotemporal correlation between the amplitude of 50- to 100-day variability and the occurrence of westward zonal flows meeting an approximate necessary condition for baroclinic instability. The notion that baroclinic instability may be involved is further corroborated by the tendency of the NEC to weaken while the eddies intensify, even as the wind works to strengthen the current.

Citation: Farrar, J. T., and R. A. Weller (2006), Intraseasonal variability near 10°N in the eastern tropical Pacific Ocean, *J. Geophys. Res.*, *111*, C05015, doi:10.1029/2005JC002989.

1. Introduction

[2] The eastern tropical Pacific is a region of great interest from the perspectives of coupled ocean-atmosphere variability and the role of the tropical oceans in weather and climate. The major oceanic and atmospheric circulations in the eastern tropical Pacific are strongly interdependent and are linked through the sea surface temperature (SST) field. The strong meridional temperature gradient in the region spanning the eastern Pacific warm pool and the equatorial cold tongue is believed to influence the strength and location of the Inter-Tropical Convergence Zone (ITCZ), and variability in the ITCZ may in turn influence the location of the jet stream and precipitation over North America [*Montroy*, 1997]. At the same time, the surface winds convergent on the ITCZ create an upwelling favorable wind stress pattern that exerts considerable influence on the strength and location of the North Equatorial Current/North Equatorial Counter Current (NEC/NECC) current system. Recent cooperative field programs in the eastern tropical Pacific, such as the Pan American Climate Study (PACS) and the Eastern Pacific Investigation of Climate (EPIC) experiment, have sought to improve understanding of the ocean dynamics that influence the evolution of SST in the eastern tropical Pacific, with the ultimate goal of improving skill in prediction of local and remote atmospheric variability driven by the SST field.

[3] Within the eastern tropical Pacific we identified the latitude band of 9–13°N as an area of particular interest and deployed a well-instrumented surface mooring there for 17 months. This latitude band is near the northernmost excursion of the meridional migration of the ITCZ and is embedded within the eastern Pacific warm pool. The mooring site was on the western edge of the eastern Pacific warm pool, a region where the SST field favors cyclogenesis [*Molinari et al.*, 2000]. In addition to kinematic and thermodynamic coupling of the ocean and atmosphere, the region near 10°N in the eastern tropical Pacific Ocean is characterized by strong intraseasonal (50- to 100-day period) sea level fluctuations; *Miller et al.* [1985] deployed a meridional array of five inverted echo sounders extending from the equator to 9°N along 110°W and found energetic 60- to 80-day dynamic height variability with an amplitude of roughly 10 dyn cm (comparable to the meridional change in dynamic height across the NECC) at the northern end of this array. There are indications of annual period variability in the strength of this intraseasonal variability; in the

[1]MIT-WHOI Joint Program in Physical Oceanography, Woods Hole Oceanographic Institution, Woods Hole, Massachusetts, USA.
[2]Department of Physical Oceanography, Woods Hole Oceanographic Institution, Woods Hole, Massachusetts, USA.

0148-0227/06/2005JC002989$09.00

14-month dynamic height time series, the oscillations were observed to be strongest during February–August [*Miller et al.*, 1985], and subsequent studies using 1–2 years of satellite altimetry data have found the variability to be strongest during roughly the first half of the year with a maximum amplitude near 10–13°N in the eastern tropical Pacific [*Perigaud*, 1990; *Giese et al.*, 1994].

[4] Strong intraseasonal velocity variability can play a role in air-sea coupling by setting the local SST and its gradient field and by effecting meridional heat transport. Near-surface meridional velocities, acting along the mean SST gradient, can cause substantial modulation of the local SST, and eddy transports can contribute to the meridional heat transport in the region. *Zhurbas and Oh* [2004] attributed elevated levels of eddy diffusivity in the eastern Pacific warm pool to heightened levels of mesoscale oceanic variability. Fluctuations in strong meridional temperature gradients can also affect the atmospheric boundary layer. The intraseasonal fluctuations in SST observed near 10°N are likely to modulate surface turbulent heat fluxes as has been noted to occur in the tropical instability wave region [*Zhang and McPhaden*, 1995; *Thum et al.*, 2002], and the SST signatures associated with eddies in the eastern Pacific warm pool [e.g., *Raymond et al.*, 2004] may be sufficient to affect atmospheric deep convection. Recent studies have also shown that intensification of tropical cyclones is influenced considerably by oceanic mesoscale SST variability [*Shay et al.*, 2000; *Hong et al.*, 2000; *Kaplan and DeMaria*, 2003], and this effect is likely to be important in the eastern tropical North Pacific, one of the world's most prolific regions of cyclogenesis. Thus, not only should the space-time nature of the energetic intraseasonal fluctuations of temperature and velocity be considered when sampling the region, but they should be considered to have potential impact on the simulation of weather and climate.

[5] While there is consensus that strong intraseasonal variability exists near 10°N in the eastern tropical Pacific, a comprehensive description of this variability is lacking. This inhibits understanding of the causes and consequences of this energetic signal. The two studies that have examined the signal over broad spatial and temporal domains [*Perigaud*, 1990; *Giese et al.*, 1994] have arrived at contradictory conclusions regarding the properties and likely generating mechanisms of the variability. While the two studies found similar phase speeds for the variability, different conclusions were reached about the origin of the sea surface height (SSH) fluctuations and the zonal direction of energy propagation. *Giese et al.* [1994] argued that the fluctuations are due to anticyclonic eddies forced by episodic wind bursts across the gulfs of Tehuantepec and Papagayo, while Perigaud suggested that the fluctuations may be due to instabilities associated with the meridional shear of the NECC and NEC. Perhaps more importantly, the two studies seem to disagree as to the nature of the fluctuations. Giese et al. argued that the motions are associated with isolated eddies that are locally forced at the eastern boundary by quasiperiodic wind events and then propagate westward, losing energy and decaying below detection threshold by about 120°W. Localized forcing at the eastern boundary implies westward energy propagation. In contrast, Perigaud treated the motions as waves (albeit nonlinear ones), and estimated the group velocity to be eastward at about 10 km/day. *Perigaud*'s [1990] inference of eastward energy propagation is inconsistent with the eastern boundary forcing mechanism proposed by *Giese et al.* [1994].

[6] Many studies have considered oceanic variability at scales of up to 1500 km in the eastern Pacific warm pool region using theoretical, numerical, or observational techniques. However, except for the work of *Miller et al.* [1985] and *Perigaud* [1990], these studies have not attempted to quantify the periodicity of the variability so it is not entirely clear whether all of these studies are relevant to the intraseasonal variability. The mountain gap winds at the gulfs of Tehuantepec and Papagayo are thought to force eddies that propagate westward (or southwestward) at speeds of about 13–17 cm/s [*Stumpf and Legeckis*, 1977; *Giese et al.*, 1994; *Ballestero and Coen*, 2004]. These eddies may be forced linearly by fluctuations in the strong mountain gap winds or nonlinearly by the annually varying winds that apply strong vorticity forcing [*Yamagata et al.*, 1990; *Umatani and Yamagata*, 1991]. *Perigaud* [1990] examined the possibility of barotropic instability in the region but did not reach any strong conclusion, and *Philander* [1976] suggested that the North Equatorial Current (NEC) may be baroclinically unstable. *Hansen and Maul* [1991] have argued that the strong anticyclonic eddies observed in the region with surface drifters result from retroflection of the North Equatorial Counter Current (NECC) at the eastern boundary. In this hypothesis, upon contact with the eastern boundary, water from the NECC moves northward to about 11°N where it takes on anticyclonic relative vorticity to conserve potential vorticity and propagates westward under the influence of the planetary vorticity gradient. Another plausible source of intraseasonal variability near 10°N is the intraseasonal coastal Kelvin wave variability in the region [*Spillane et al.*, 1987; *Enfield*, 1987], which may radiate Rossby waves to the west.

[7] Some authors have interpreted the literature on this variability as evidence of distinct types of variability [e.g., *Weidman et al.*, 1999] while others have treated the different observational studies as evidence of a single type of intraseasonal variability [e.g., *Giese et al.*, 1994]. The various theories for the strong intraseasonal variability on 10–13°N can be grouped into four classes: (1) mountain gap wind forcing of intraseasonal eddies, either by fluctuating or seasonally varying winds, (2) instability of the zonal equatorial currents, either by barotropic instability (involving the NEC/NECC shear) or baroclinic instability (involving the vertical shear of the NEC), (3) NECC retroflection, and (4) radiation of Rossby waves (or similar westward propagating variability) from the intraseasonal coastal Kelvin waves that exist on the eastern boundary. The present study seeks to develop a more complete characterization of the intraseasonal variability near 10°N in the eastern tropical Pacific by drawing on both in situ and satellite data.

[8] In this paper, we analyze in situ current and dynamic height data, satellite SST, and satellite altimetry to gain further insight into the energetic intraseasonal oscillations along 10°N in the eastern tropical Pacific. This paper is organized as follows: Section 2 provides an overview of the data used, and section 3 gives a qualitative description of the intraseasonal fluctuations as seen in in situ data and examines the effects of the variability on SST. Section 4 uses satellite SST and satellite altimetry to complete this description and set the broader spatial and temporal context.

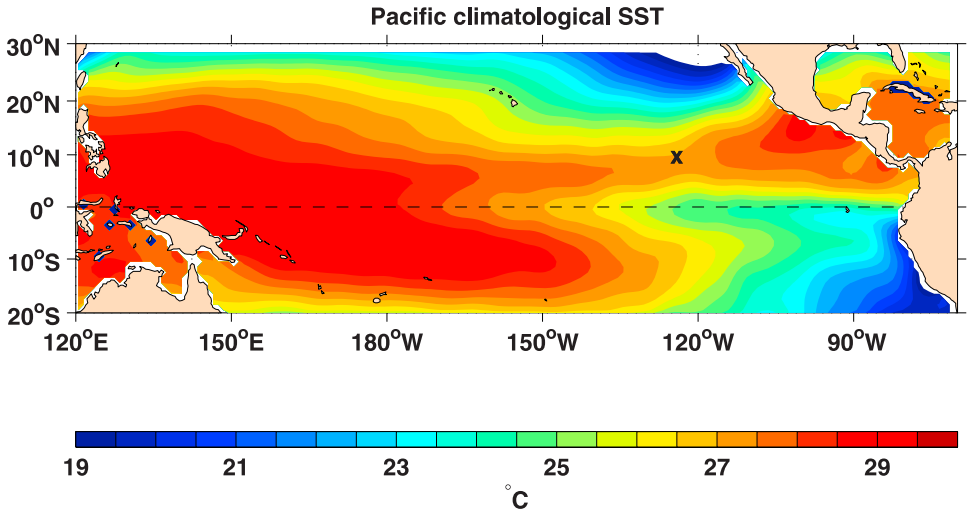

Figure 1. Mean SST of the tropical Pacific [*Levitus and Boyer*, 1994]. The location of the mooring is indicated by a cross at 10°N, 125°W.

Section 5 quantifies basic properties of the variability, such as its wavelength, frequency, and dispersion relation. Section 6 discusses the interpretation of the intraseasonal oscillations as Rossby waves and the generation mechanisms for the variability. Finally, section 7 offers some concluding remarks.

2. Data

[9] As part of the NOAA-funded PACS experiment, two stations in the eastern tropical Pacific were occupied by surface moorings from May 1997 to September 1998 [*Anderson et al.*, 2000]. In this paper we use data from the mooring deployed at 10°N, 125°W (Figure 1); the other mooring was placed at 3°S, 125°W in the Equatorial Cold Tongue.

[10] Because of power and data storage constraints, the moorings were recovered and replaced in December 1997. With temporal resolution of 15 minutes or better, meteorological packages on the mooring provided accurate time series of surface variables used to compute air-sea fluxes of freshwater, heat, and momentum via the bulk flux algorithms of *Fairall et al.* [1996]. Each mooring carried a Vector Averaging Wind Recorder or VAWR [*Weller and Anderson*, 1996] and an Improved METeorological system (IMET [*Hosom et al.*, 1995]). Temperature, salinity, and velocity measurements were obtained with closely spaced instruments attached to the mooring line in the upper 200 m of the ocean. Temperature was recorded at 30 depths, and eight conductivity-temperature recorders were located in the upper 80 m. Ten Vector Measuring Current Meters (VMCMs [*Weller and Davis*, 1980]) were located at depths between 5 and 110 m during the first deployment, and nine VMCMs were located between 10 and 110 m during the second deployment. Temperature, conductivity, and velocity were sampled with a temporal resolution of 15 minutes or better. Some sensors were damaged by fishing line; particularly, three temperature-conductivity recorders were destroyed during the first deployment. More detail about the moorings, the cruises, and the data processing is available in technical reports [*Way et al.*, 1998; *Trask et al.*, 1998; *Ostrom et al.*, 1999; *Anderson et al.*, 2000].

[11] This study also makes use of SST and SSH products derived from satellite measurements. We use Version 3 of the 0.5°, 5-day binned SST from the Advanced Very High Resolution Radiometer (AVHRR) on the NOAA polar orbiting satellites distributed in association with the World Ocean Circulation Experiment (WOCE). For quantitative spectral calculations involving altimetry data, we use the WOCE Version 3 0.5°, 10-day binned TOPEX/Poseidon SSH anomaly data set. We use the WOCE Version 3 1°, 5-day gridded and interpolated TOPEX/Poseidon SSH anomaly data set for display purposes (i.e., in figures showing SSH anomaly) and when computing SSH anomaly gradients. The SSH anomaly and SST products used here and details regarding their processing can be obtained from the NASA Jet Propulsion Laboratory Physical Oceanography Distributed Active Archive Center web site at "http://podaac.jpl. nasa.gov/woce/". For all calculations utilizing the AVHRR SST data, gaps caused by clouds were filled by linear interpolation in time. This approach was chosen because the data gaps typically span fewer data points in time than in space, lasting for times comparable to atmospheric synoptic timescales.

[12] We also employ the *Bonjean and Lagerloef* [2002] tropical Pacific surface current analysis to understand the spatial and temporal context of the low-frequency (seasonal timescale) currents measured at the mooring site. These investigators used a diagnostic model incorporating geostrophic, Ekman, and thermal wind dynamics to estimate the surface currents (15 m depth) from SSH anomalies, SST, surface winds, and mean dynamic topography. It is noteworthy that the Bonjean and Lagerloef analysis does show an intraseasonal signal at the mooring site that is in phase with the observed signal; however, the amplitude of the signal is too small during the spring of 1998, presumably because the objectively analyzed, $1° \times 1°$ version of the TOPEX/Poseidon data used for their analysis further smooths the 5° signal (section 5) that is already only marginally resolved in TOPEX/Poseidon data, which has a zonal track separation of up to 316 km. Although intra-

seasonal variability in the currents at the mooring site is not adequately represented in the surface current analysis, the *Bonjean and Lagerloef* [2002] currents seem to give a faithful representation of the zonal current at lower frequencies. For example, the mean zonal current in the *Bonjean and Lagerloef* [2002] analysis at the mooring site during the mooring deployment differs from the in situ mean at 15 m depth by only 1.1 cm/s. Given the strong intraseasonal variability and the relatively short 17-month mooring record, this agreement may be fortuitous, but, for lack of a better estimate, we will use the *Bonjean and Lagerloef* [2002] surface currents when considering the spatial and temporal variability of the low-frequency zonal currents.

[13] We will discuss a number of period bands in this paper. The period band of interest is 50–100 days, but when working with the relatively short 504-day mooring record, it is sometimes impractical to examine the full 50- to 100-day period band. This is especially true when performing band-pass filtering or spectral computations on the mooring data. When band-pass filtering the mooring data, we face a tradeoff in selection of low-frequency cutoff for the passband. A lower frequency cutoff passes more intraseasonal energy, but also shortens the useful length of the band-passed record. This tradeoff motivates our choice of passband low-frequency cutoffs, which will be chosen according to circumstance. We choose the high-frequency cutoff to be as high as possible while still suppressing energy in the internal wave and atmospheric weather bands in order to make the passband as broad as possible to avoid unwanted distortions by a narrow band filter. All data filtering is done with a moving average filter. When performing spectral calculations on the mooring data, the ''intraseasonal band'' is dictated by the record length and the amount of averaging required to obtain statistically meaningful results.

3. Intraseasonal Variability at the Mooring

[14] For comparison with the dynamic height observations of *Miller et al.* [1985] at 9°N, 110°W, we computed the steric height of the water column between 10 and 110 m depths using the temperature and salinity data from the mooring. Because of conductivity sensor failures during the first phase of the field program, the salinity at depths where no data were available was estimated by linear regression between observed temperature and salinity. The 20° isotherm (a proxy for the center of the thermocline) was always shallower than 110 m, so the 10–110 m depth interval covers a substantial fraction of the density difference over the water column. The steric height, filtered to pass 21- to 91-day variability, is shown in Figure 2. While the amplitude of the steric height signal, computed between 10 and 110 m depths, cannot be quantitatively compared to the full water column dynamic height observations of *Miller et al.* [1985], the seasonal modulation of the signal is remarkably similar to that observed by *Miller et al.* [1985], with the strongest intraseasonal variability occurring between January and August 1998. The period of the oscillations can be seen to be about 2 months from October 1997 to June 1998, and the oscillations rapidly intensify during the first few months of 1998. The amplitude of the oscillations approximately doubles between December 1997 and February 1998, and it doubles again between February and April 1998. At its peak strength in April 1998, the signal is associated with nearly a 7 cm peak-to-peak change in the thickness of the upper 110 m of the water column.

[15] Strong intraseasonal current fluctuations are evident within the mixed layer and are coincident with the signal in steric height (Figures 3 and 4). A 10-day averaging period was chosen to emphasize the subinertial variability, as the inertial period is about 2.87 days at 10°N. Above the thermocline, intraseasonal variability was found in the zonal currents as well as in the meridional currents. However, the upper ocean zonal and meridional currents are not significantly coherent at intraseasonal frequencies. Below the thermocline, zonal and meridional velocity components are also incoherent at subinertial frequencies. The meridional velocity (Figure 4) shows strong oscillations with a period of about 2 months during November 1997 to July 1998. While the subthermocline meridional velocity clearly exhibits a quasiperiodic signal with a period of roughly 2 months between November and July, the zonal velocity is dominated by lower frequency variability, as can be seen in the velocity time series from the deepest current meter at 110 m depth (Figure 5). Aside from two periods of strong near-surface zonal currents in May 1997 and July 1998, the low-frequency meridional currents are comparable in size to the zonal currents above the thermocline; both are typically 10 to 20 cm/s (Figure 4). The westward velocity signal observed during May/June 1997 was associated with the passage of an anticyclonic eddy that approached from the east (shown in section 6.2); the peak velocity signal associated with this eddy was 40–50 cm/s in the upper 40 m and more than 15 cm/s at 110 m.

[16] The nonstationarity of the intraseasonal oscillations is evident, and conventional spectral analysis of the time series does not recover a discrete, statistically significant spectral peak associated with them. To better quantify the temporal evolution of the energy levels at different periods we used the wavelet power spectrum. Figure 6 shows the wavelet power spectrum for the meridional velocity at 110 m (10°N, 125°W) computed using a Morlet wavelet following *Torrence and Compo* [1998]. In Figure 6, the parabola-like yellow line indicates the cone of influence; below this curve, edge effects may contaminate the spectrum [*Torrence and Compo*, 1998]. This analysis reveals a distinct spectral peak that transitions from a period near 85 days in October/November 1997 toward a period near 50 days by June 1998 (Figure 6).

[17] The intraseasonal velocity fluctuations at the mooring site were accompanied by substantial fluctuations in SST during part of the observational record. While this coherence of SST and meridional velocity is apparent in the raw data, the relationship is more readily apparent when comparing the 20- to 70-day band-passed meridional velocity at 10 m depth and the 20- to 70-day band-passed SST (25 cm depth) from the mooring site (Figure 7). From January to June 1998, there is a signal in SST with an amplitude of 0.2–0.4°C. These observations are reminiscent of the work of *Leeuwenburgh and Stammer* [2001], who found significant correlations of SST and the ocean eddy/wavefield on timescales as short as 1 month and attributed

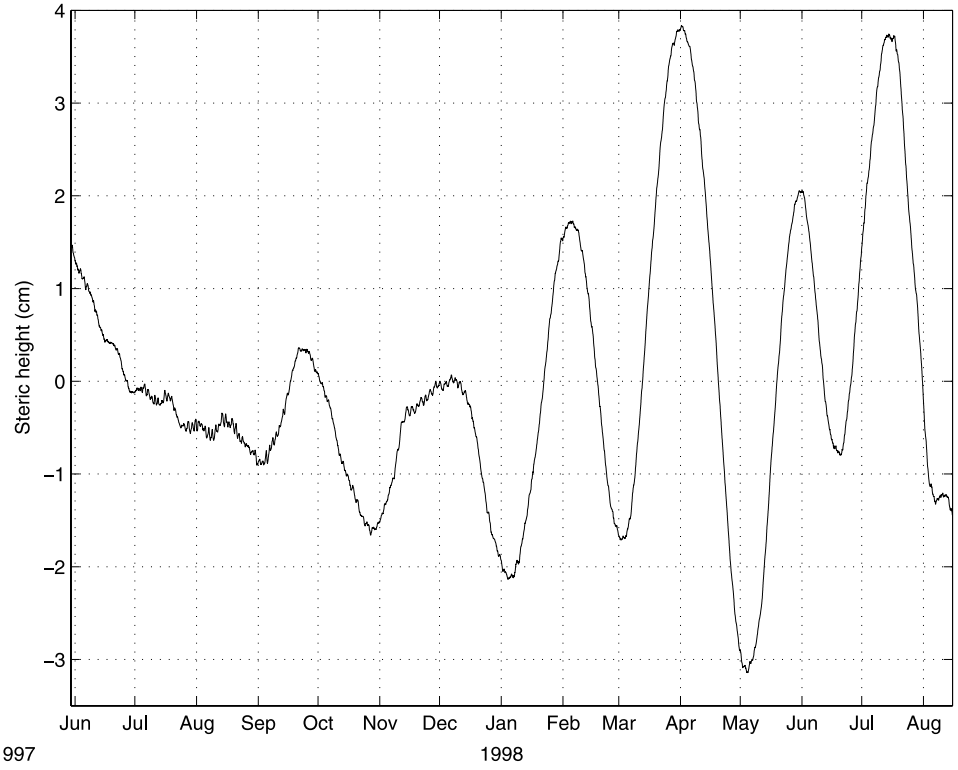

Figure 2. The 21- to 91-day band-passed steric height at 10 m relative to 110 m. Edge effects in the filtering contaminate the signal prior to 1 August 1997 and after 15 June 1998.

these correlations to advection by the geostrophic eddy/wavefield.

[18] The peak-to-peak change in SST associated with this signal was observed to exceed 0.8°C at the mooring site, so it is of interest to determine the extent to which horizontal advection can account for the signal. The evolution of temperature is governed by conservation of heat, given approximately by

$$\frac{\partial T}{\partial t} = \frac{\nabla \cdot \mathbf{q}}{\rho c_p} - (\mathbf{u} \cdot \nabla T), \tag{1}$$

where ρ is the density of seawater, c_p is the specific heat, and $\mathbf{q}$ is the turbulent and radiative heat flux. To understand the balance of processes that set SST, the typical procedure is to combine the equations of heat and mass conservation and integrate vertically over the mixed layer [e.g., *Cronin and McPhaden*, 1997]. However, since our primary interest here is in understanding the effect of horizontal advection on SST, we examine the balance of the tendency of SST with the advection term directly.

[19] We carried out the analysis at 10 m depth, since this is the shallowest depth where both temperature and currents are available for both phases of the field program. We estimated the horizontal surface temperature gradient, ∇T, at 5-day resolution by a fourth-order-accurate centered difference scheme using the WOCE Version 3 AVHRR SST product and linearly interpolated the $0.5^\circ \times 0.5^\circ$ field to the mooring location. This type of approach to estimating ∇T is believed to provide a reasonably accurate estimate of the mixed layer horizontal temperature gradient [*Wang and McPhaden*, 1999, 2001]. To suppress noise in the ∇T estimate due to measurement error and unresolved variability in the SST field and its subsequent amplification in the discretized derivative, we smoothed the ∇T estimate in time with an 11-point (55-day) running average filter. As such, only the contributions of the low-frequency ∇T are included in the calculation.

[20] The zonal temperature gradient was considerably weaker than the meridional temperature gradient (Figure 8a). The meridional temperature gradient reached −0.86°C/° latitude during May 1998 in the final stage of the 1997–1998 El Niño event, whereas the magnitude of the zonal temperature gradient never exceeded 0.25°C/° longitude during the mooring deployment. During May–November 1997, SST gradients were relatively small, the mixed layer was relatively shallow, and the presence of the ITCZ at the site contributed to variability in the surface meteorology, so that SST was more heavily influenced by entrainment and variability in the surface heat fluxes than by horizontal advection during this time period. Zonal advection was relatively unimportant except during the periods of strong zonal flow during June/July 1997 and July 1998 (Figure 8b). In contrast, meridional advection by the intraseasonal velocity signal exerted considerable influence on mixed layer temperature during February to June 1998. As noted earlier, the zonal and meridional currents were typically of comparable strength, but the meridional advection term exerted a sustained influence on SST because it was acting more nearly along the mean temperature gradient (Figure 8b). Thus the

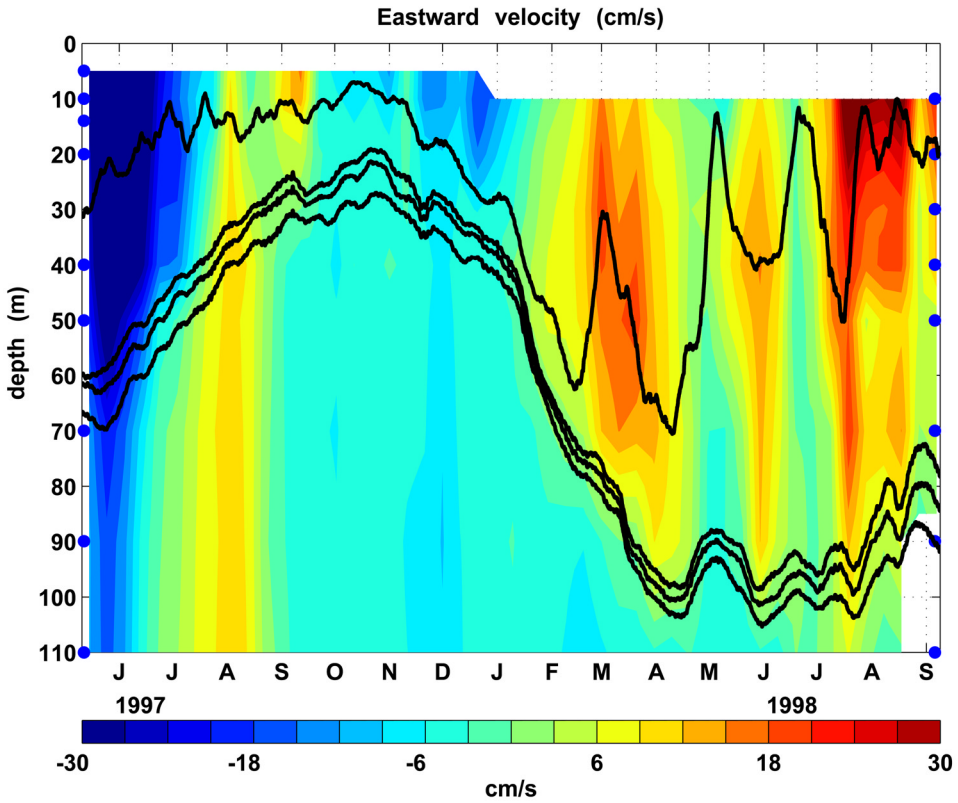

Figure 3. Depth-time plot of 10-day averaged zonal velocity at 10°N, 125°W. Current meter locations during the two deployments are indicated by blue dots on the left and right edges. The upper black line indicates the mixed layer depth (where the temperature is 0.1°C less than its surface value), and the lower three black lines are isotherms in the upper half of the thermocline (19, 22, and 24°C isotherms). Mixed-layer depth and isotherms are 10-day running averages.

intraseasonal signal in meridional velocity played an important role in setting the sea surface temperature during most of the first half of 1998.

4. Intraseasonal Variability Near 10°N in the Eastern Tropical Pacific

[21] The presence of coherent SST and velocity signals at the mooring site indicated that information about the spatial characteristics of the intraseasonal signal might come from satellite measurements of SST. Longitude-time plots of SST and SST filtered to pass 50- to 100-day period, 2–15° wavelength variability along 10.25°N from the WOCE AVHRR SST data set reveal the presence of westward propagating signals with phase speeds of 8–18 cm/s (Figure 9). The intraseasonal signal is evident at the mooring site (125°W) and over a broad range of longitude. The wavelength at the mooring site appears to decrease through time from about 15° longitude during the early part of the mooring record to about 5° by the spring of 1998. By inspection, the westward phase speed at the mooring site during March and April 1998 is estimated to be about 10 cm/s.

[22] The broad spatial and temporal coverage of the TOPEX/Poseidon satellite allows examination of the spatial and temporal structure of the fluctuations in SSH associated with the intraseasonal fluctuations in currents, dynamic height, and SST. The previous work of *Perigaud* [1990] and *Giese et al.* [1994] found that intraseasonal SSH signals near 10°N propagate westward. A longitude-time diagram of zonal slope of SSH anomaly also clearly shows westward propagating variability with intraseasonal periods and wavelengths of roughly 5–15° (Figure 10). To the extent that the intraseasonal SSH anomaly signals are resolved in the altimetry data, the zonal slope of SSH anomaly is expected to be proportional to the intraseasonal meridional velocity signal. By inspection, the phase speed of the signal ranges over roughly 8–18 cm/s and the maximum zonal gradients of SSH tend to occur in the eastern Pacific during the boreal spring. Note that the intraseasonal signal observed at the mooring (and in satellite SST) during the spring of 1998 is not clearly reflected in Figure 10, probably because the short wavelength of the signal (about 5° of longitude) is not well resolved in the 1° gridded TOPEX/Poseidon data used for the plot.

[23] An estimate of the distribution of intraseasonal power in time and space is desirable because it can give insight into the generation location of the variability and the zonal direction and speed of energy propagation. One way of producing such an estimate is to compute the wavelet frequency spectrum for SSH at each point in longitude to yield an estimate of intraseasonal SSH power through time and longitude. We computed the wavelet power spectrum of SSH for each location along 10.25°N and extracted time

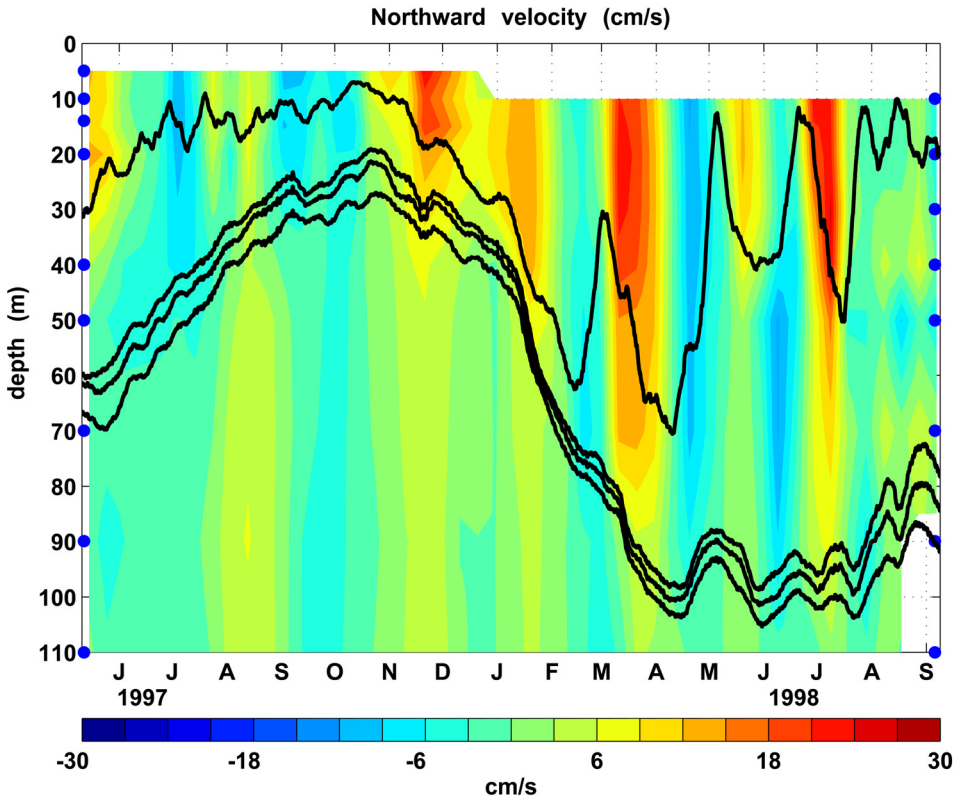

Figure 4. Depth-time plot of 10-day averaged meridional velocity at 10°N, 125°W. Current meter locations during the two deployments are indicated by blue dots on the left and right edges. The upper black line indicates the mixed layer depth (where the temperature is 0.1°C less than its surface value), and the lower three black lines are isotherms in the upper half of the thermocline (19, 22, and 24°C isotherms). Mixed-layer depth and isotherms are 10-day running averages.

series of power in the 50- to 100-day band. Then, we averaged the 50- to 100-day power estimates over pairs of adjacent longitude points (0.5° apart) to improve the stability of the estimate and took the square root to obtain a time series of 50- to 100-day amplitude for each point (Figure 11). As expected from prior work and the observations discussed here, the amplitude is largest east of 120°W and is annually modulated. The westward group speed of first baroclinic mode, long Rossby waves at this latitude in the eastern Pacific is about 20 cm/s, taking the value of the deformation radius to be the zonal mean of the values reported by *Chelton et al.* [1998] for 88–115°W. This speed, indicated in Figure 11, can be thought of as a realistic upper bound on the westward group velocity of baroclinic motions in the region. Although faster westward group speeds are theoretically possible, they require unrealistically large westward current speeds. Most of the localized amplitude peaks in the region appear to travel westward at speeds less than the long Rossby wave group speed (e.g., the peak originating near 105°W at the beginning of 1994), consistent with westward energy propagation. During most years, multiple amplitude peaks appear nearly simultaneously across a fairly broad range of longitude (up to 20°). The increase of energy over such a broad range of longitude is too rapid to be attributable to baroclinic wave propagation from the east. A possible exception is 1998, when an amplitude peak can be seen to travel westward from near the eastern boundary to about 125°W; this different behavior may be related to the transition of the tropical Pacific to a La Niña state after the strong El Niño of 1997–1998.

[24] To clarify the temporal variability in the region, the estimates of the wavelet power spectrum of SSH anomaly at each longitude along 10.25°N were averaged into three bins of about 15° longitude within the eastern tropical Pacific. The RMS amplitude of 50- to 100-day variability along 10.25°N was computed by taking the square root of the mean SSH 50- to 100-day power at each longitude (Figure 12d). The peak RMS amplitude occurred in the middle bin (100–115°W) and there was a slightly lower peak amplitude in the easternmost bin (88–100°W). In the westernmost bin (115–130°W) the RMS amplitude was substantially smaller than in the two bins to the east, but was above the background level of the central Pacific. As expected from earlier observations of intraseasonal SSH variability in the region [*Miller et al.*, 1985; *Perigaud*, 1990; *Giese et al.*, 1994], the amplitude of the 50- to 100-day variability undergoes a substantial annual cycle, with peak amplitudes during roughly the first half of each year. During each of the years 1993–2001, the peak amplitude in each subregion occurs between February and July (Figure 12). In the easternmost bin (88–100°W) the peak amplitude occurred most often in March, while in the middle bin (100–115°W) the

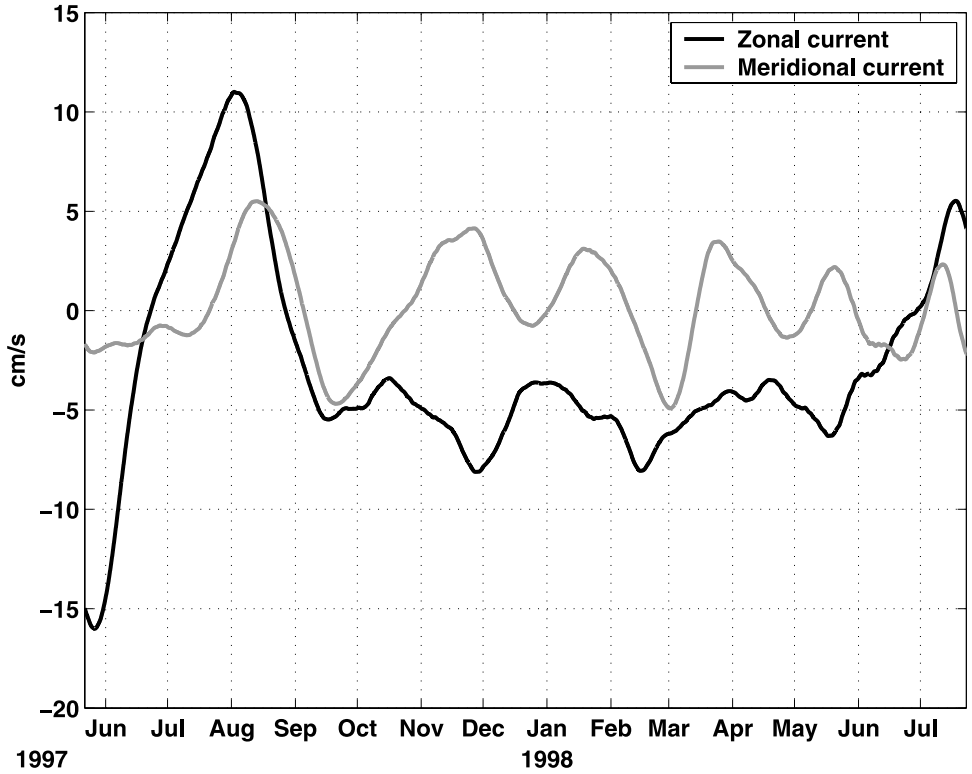

Figure 5. Zonal and meridional velocity components at 110-m depth. Both time series have been smoothed by two successive applications of an 11-day moving average filter.

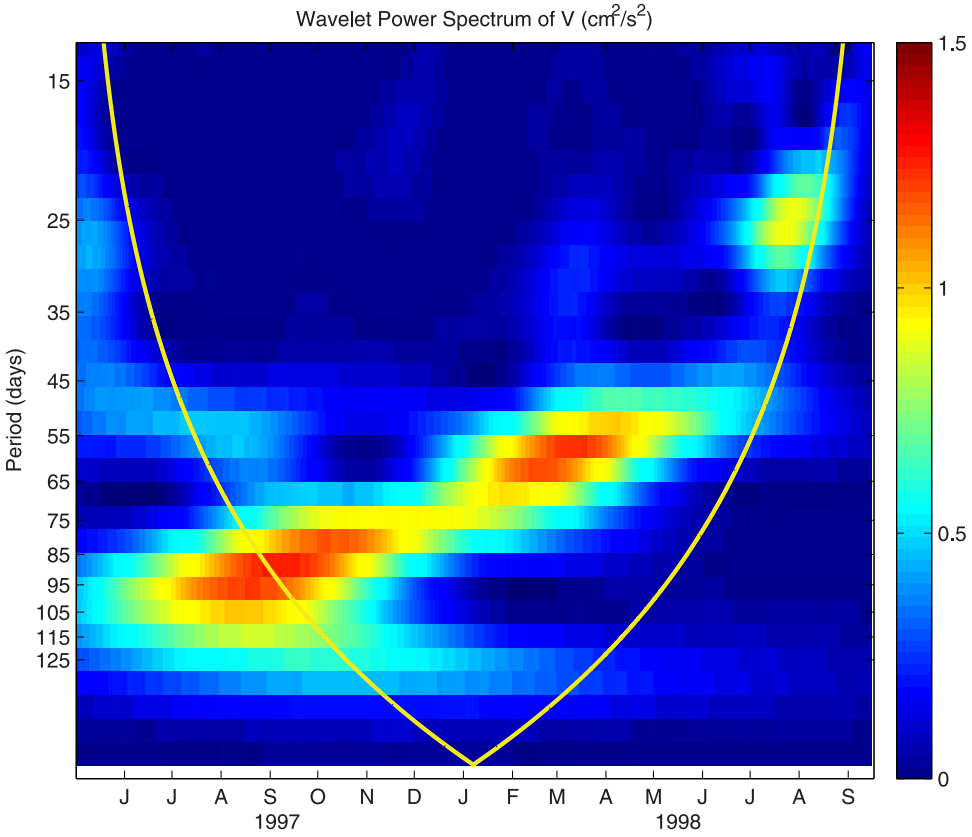

Figure 6. Wavelet power spectrum of the meridional velocity at 110 m (cm^2/s^2). The solid yellow curve indicates the cone of influence; below this curve edge effects potentially contaminate the results.

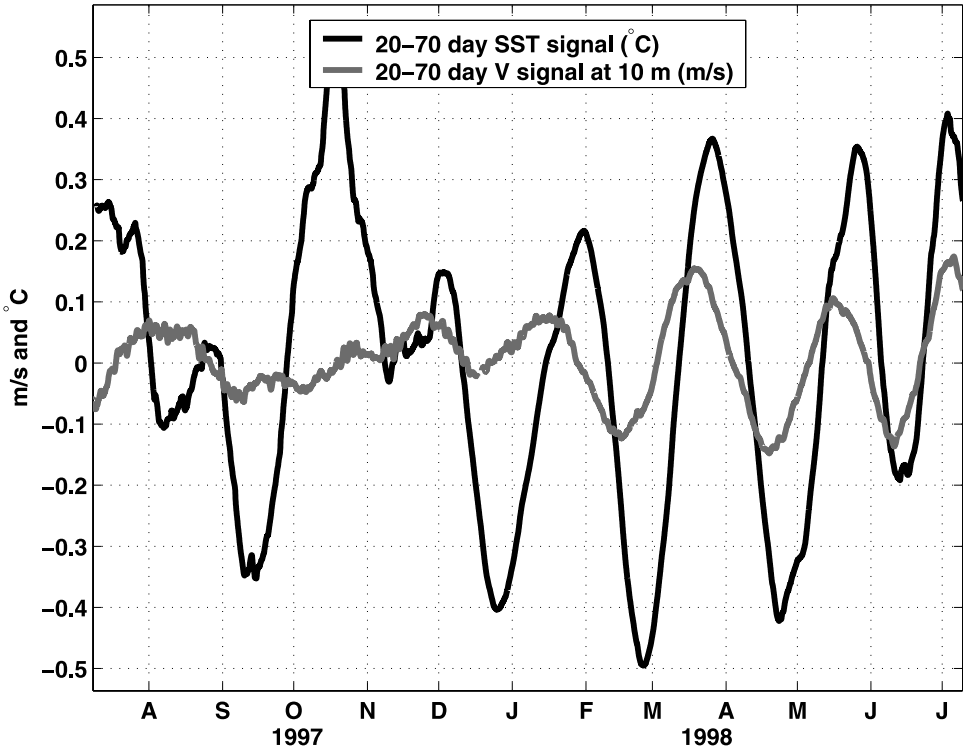

Figure 7. SST and 10-m velocity from a mooring at 10°N, 125°W, filtered to pass 20- to 70-day variability.

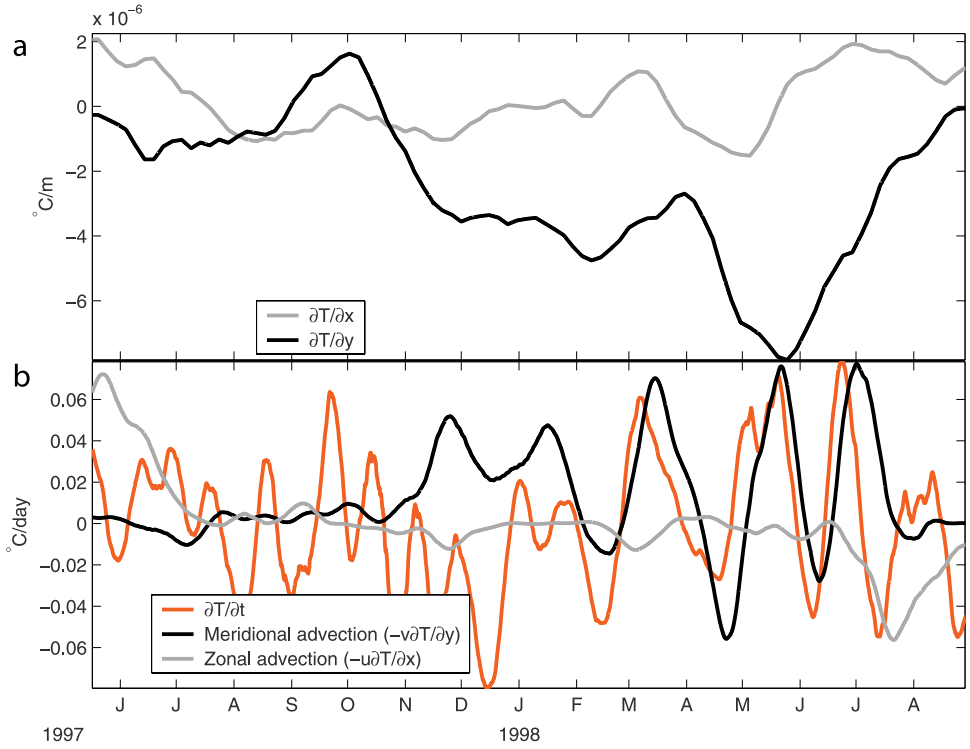

Figure 8. (a) Zonal and meridional components of the surface temperature gradient at 10°N, 125°W (grey and black lines, respectively). (b) Estimated contribution of zonal advection (grey line) and meridional advection (black line) to the local rate of change of surface temperature (red line). In Figure 8b, all quantities were smoothed by two successive applications of an 11-day moving-average filter.

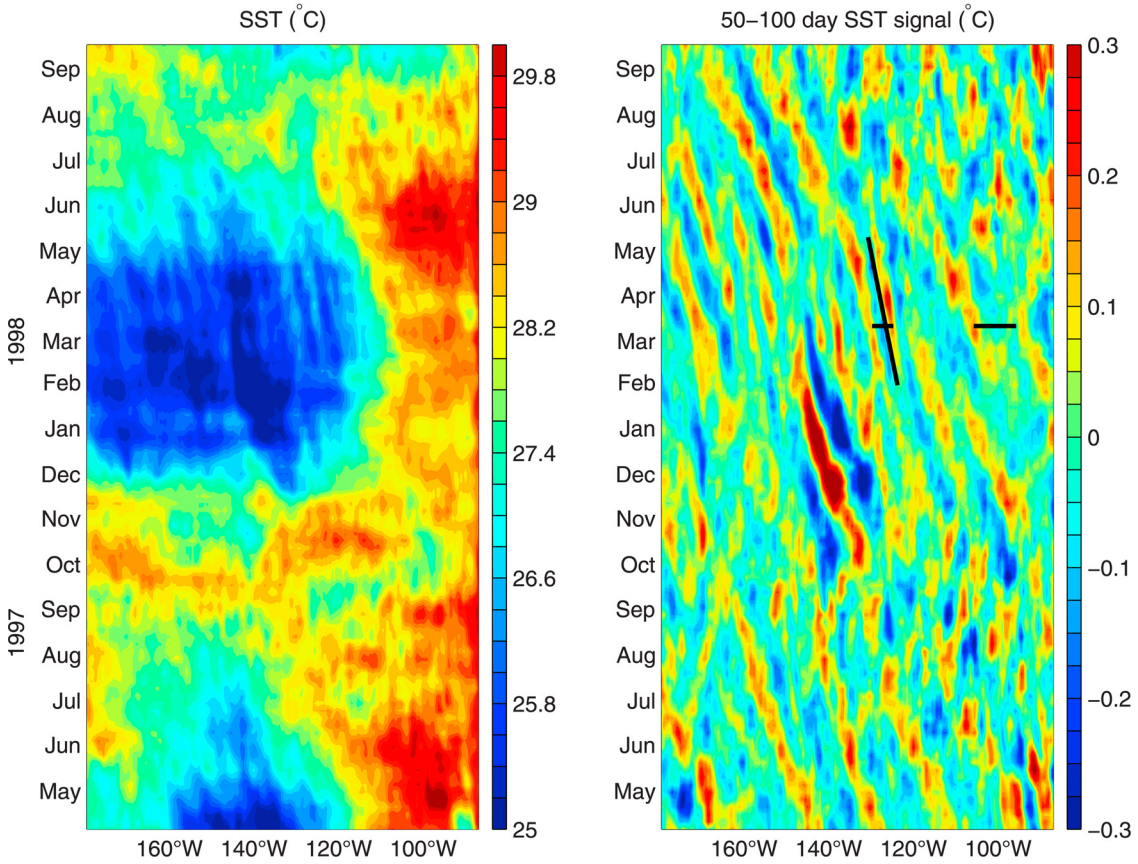

Figure 9. (left) AVHRR SST along 10.25°N. (right) The 50- to 100-day SST signal along 9.75°N. In Figure 9 (right), a 15° longitude zonal running average was removed to filter SST fluctuations of larger zonal scales. The mooring was located at 125°W. For reference, zonal scales of 5° and 10° longitude are marked in March 1998. The solid diagonal line indicates a westward speed of 10 cm/s.

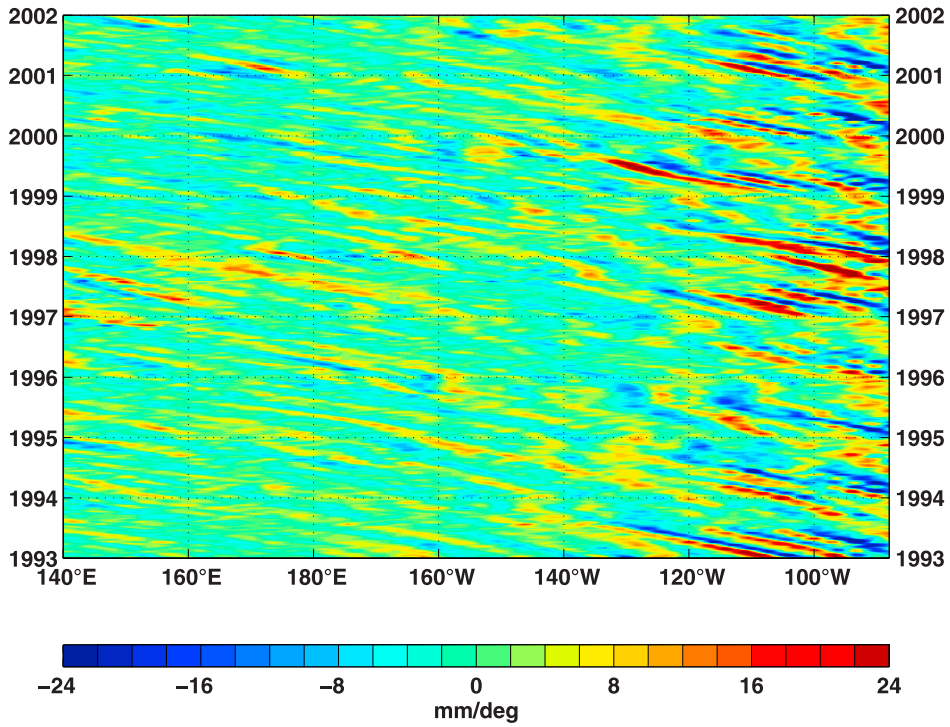

Figure 10. Zonal slope of SSH anomaly along 10.5°N. No filter was applied.

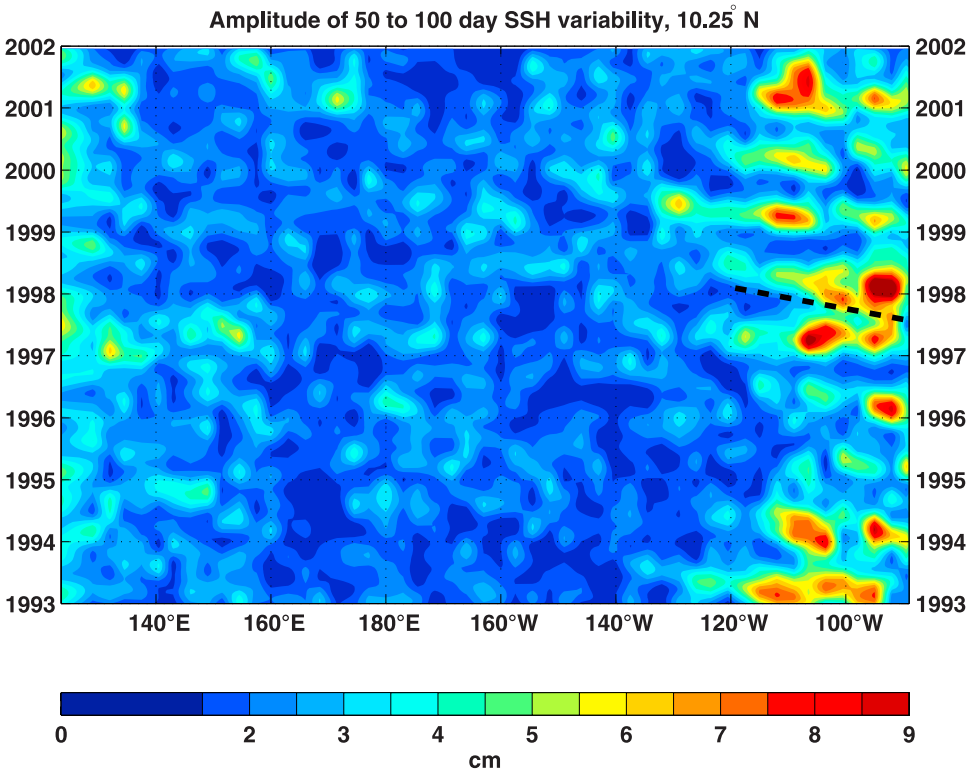

Figure 11. Longitude-time plot of amplitude of 50- to 100-day variability along 10.25°N in the tropical Pacific Ocean based on wavelet analysis of TOPEX data from 1993 to 2001. The time-longitude evolution of amplitude provides an indication of the speed of zonal energy propagation. The thick dashed line indicates a realistic upper bound on the westward group speed for baroclinic Rossby waves in the eastern tropical Pacific (i.e., the long wave speed). During most years, the amplitude increases too rapidly to be attributable to a baroclinic signal that propogated due westward from the eastern boundary. Note that the tropical Pacific was undergoing transition from a strong El Niño to a strong La Niña during early 1998, and it appears that some of the 50- to 100-day amplitude may have propagated well offshore from the eastern boundary during that time period.

peak amplitude occurred most often in April, and in the westernmost bin (115–130°W) the amplitude peaked most often in May.

[25] The temporal evolution over 1993 to 2001 of SSH anomaly amplitude in these three longitude bins in the 50- to 100-day period band is shown in Figure 13. The amplitude is typically larger in the 100–115°W region than in the 88–100°W or 115–130°W regions; only during 1998 was the amplitude substantially larger in the bin nearest to the eastern boundary. The intraseasonal fluctuations appear to have been less energetic in 1995 and 1996 than in other years. This year-to-year variability may explain the different amplitudes of intraseasonal variability near 10°N in the eastern tropical Pacific reported in prior studies. *Miller et al.* [1985] reported amplitudes of about 10 dyn cm; *Perigaud* [1990] reported a maximum SSH amplitude of 6.9 cm; and *Giese et al.* [1994] reported amplitudes of 5–13 cm. (Giese et al. actually reported 10–25 cm, but we take that to mean peak-to-peak amplitude; see their Figure 3b.) While differences filtering and signal processing in the various studies can probably account for part of the difference in reported amplitudes, the 9 year time series in Figure 13 suggests that much of the difference in observed amplitudes may be due to the intrinsic spatial and interannual variability of the amplitude of the intraseasonal signal.

5. Estimation of Spatial Scales and Propagation Characteristics

[26] In this section, we present quantitative estimates of the zonal wavelength and phase speed of the intraseasonal signal and investigate characteristic frequencies and wave numbers along 10°N using TOPEX/Poseidon SSH data and the in situ mooring data. The zonal wave number–frequency spectrum was estimated using a two-dimensional fast Fourier transform (2DFFT), by a method similar to that described by *Zang et al.* [2002], applied to the WOCE Version 3.0 0.5° gridded TOPEX/Poseidon product for the period of 1993–2001. Since the TOPEX/Poseidon satellite generally does not provide data at zonally uniform sampling intervals, the data were first linearly interpolated to the smallest zonal sampling interval. The temporal mean was removed from the sea surface height anomaly before computing the 2DFFT at 9.75, 10.25, and 10.75°N over 140°E–88°W. The points in each periodogram were multiplied by the square of the

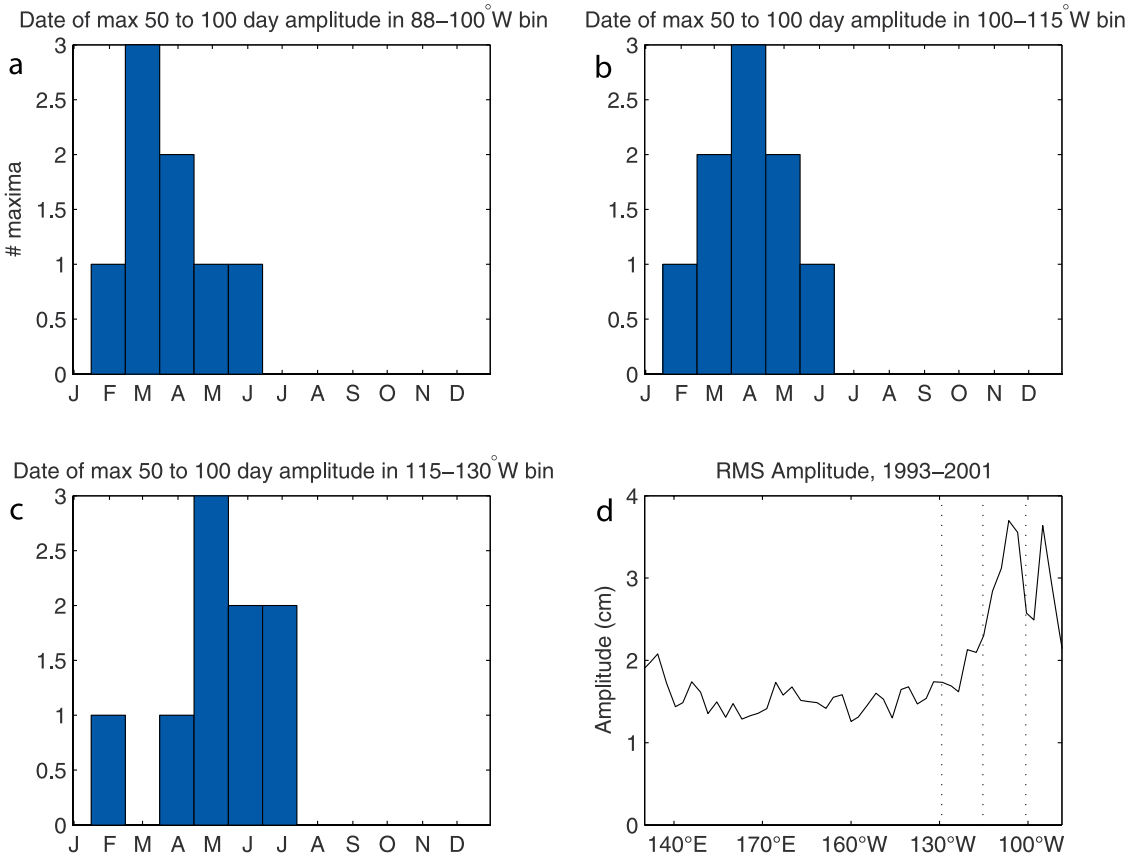

Figure 12. (a), (b), and (c) Histograms showing the time of peak amplitude of 50- to 100-day variability during each year at 10.25°N for three subregions of the eastern tropical Pacific Ocean based on wavelet analysis of TOPEX data from 1993 to 2001. (d) RMS amplitude of 50- to 100-day variability as a function of longitude during 1993–2001.

wave number to obtain periodograms for zonal sea surface slope. The zonal slope of SSH anomaly is taken to be a proxy for upper ocean meridional velocity. The three 2-D periodograms, assumed to have uncorrelated noise, were averaged to improve the statistical stability of the spectral estimate. Then, nonoverlapping averaging was carried out across seven adjacent frequency bands and three wave number bands. This leads to a total of 125 degrees of freedom and a 95% confidence interval (in a chi-square sense) of 0.22 decibels. To allow for the possibility that the three periodograms are heavily dependent, we also computed a more pessimistic 95% confidence interval for 41 degrees of freedom (0.38 decibels). We will report results based on this second confidence interval.

[27] The resulting wave number-frequency spectrum of SSH zonal slope along 10.25°N shows elevated variance in the 50- to 100-day period band (Figure 14). In Figure 14, westward propagating signals have negative wave numbers. As might be expected, most of the energy in sea surface slope along 10°N is associated with westward propagating signals. Most of the energy at periods of 40–70 days has zonal wavelengths of 5–9°, while most of the energy at periods of 75–100 days exists at somewhat larger zonal scales of 6–20°. Within the 10 frequency bands in the 42- to 102-day period band, the maximum spectral power at each frequency lies at wavelengths between 5.8 and 13.2° longitude. Statistically significant power is found with a broad range of phase speeds, but the spectral peaks all occur at phase speeds of 10–20 cm/s. The intraseasonal variability is not significantly stronger than the semiannual variability when the more pessimistic confidence interval is employed. Even so, *Perigaud* [1990] showed that the intraseasonal power in SSH anomaly on 10–14°N in the eastern Pacific is substantially higher than in the western Pacific or in the eastern tropical South Pacific. The wave number-frequency spectrum is a measure of the average power over the spatial and temporal domain indicating that, on average during 1993–2001, the most energetic variability in (resolved) sea surface slope in the 40- to 100-day period band propagates westward with a wavelength of 5–15°. Note that the enhanced power levels at ±4° wavelengths are an artifact of linear interpolation of the nonuniformly spaced zonal sections to a uniform grid.

[28] We can take advantage of the dynamics that govern variability at frequencies much less than the local inertial frequency to further refine an estimate of the wave number and phase speed of the intraseasonal signal observed at the mooring site. For low frequency motions (frequencies much less than inertial) that are not directly wind driven, the

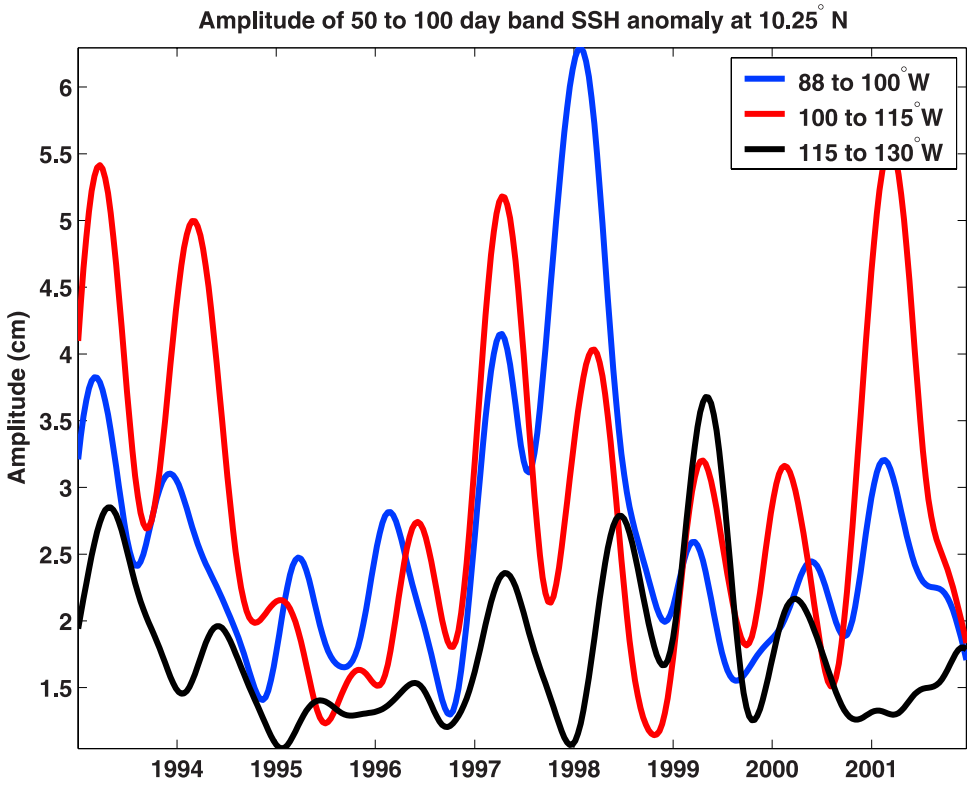

Figure 13. Estimated amplitude of 50- to 100-day variability in SSH anomaly at 10.25°N for three subregions of the eastern tropical Pacific Ocean. Edge effects potentially contaminate the results during about the first and last 140 days of each time series.

meridional velocity is very nearly geostrophic [e.g., *Gill*, 1982]. That is,

$$v = \frac{g\eta_x}{f}, \tag{2}$$

where η is the dynamic height, v is the meridional velocity (relative to the velocity at the reference level for the dynamic height), and the subscript denotes partial differentiation. Supposing that variability at each frequency is associated with only one zonal wave number, the zonal phase speed is given by

$$c_p(\omega) = \frac{\omega}{k} = \frac{\hat{\eta}_t}{\hat{\eta}_x}, \tag{3}$$

where $\hat{\eta}_t$ and $\hat{\eta}_x$ are the complex Fourier amplitudes of η_t and η_x, ω is the frequency, and k is the zonal wave number. The phase speed, $c_p(\omega)$, can be thought of as the transfer function (or frequency response function) between dynamic height tendency and dynamic height zonal slope [cf. *Bendat and Piersol*, 1986]. Using equation (2), we can rewrite equation (3) as

$$\hat{\eta}_t = H(\omega)\hat{v}, \tag{4}$$

where $H(\omega) = c_p f/g$ is the transfer function between dynamic height tendency and meridional velocity. This term can be estimated empirically from the mooring data to determine the value of $c_p(\omega)$. This approach was employed by *McPhaden* [1996] to estimate the phase speed and wave number of monthly period variability observed at a mooring in the tropical Pacific.

[29] Following *McPhaden* [1996], we calculated the dynamic height relative to 110 m, the deepest current meter depth (section 3). Then, the meridional velocity was referenced to that at 110 m depth to obtain the time series v, and the dynamic height tendency, η_t, was calculated by a fourth-order-accurate centered difference scheme. The empirical transfer function, H, was then computed as described by *Bendat and Piersol* [1986]. Specifically, $H(\omega) = \gamma_{(\eta t,v)}\sqrt{R}e^{-i\phi}$, where $\gamma_{(\eta t,v)}$ and ϕ are the coherence amplitude and phase of η_t and v, and R is the ratio of the power spectral densities of η_t and v. Then, the phase speed is given by c_p = Real($\frac{gH}{f}$). Note that the transfer function is defined in terms of the coherent variability in v and η_t, so that uncorrelated noise in the measurements of v and η_t does not contribute to H. Furthermore, if another forcing term contributes to variability in v in equation (2) (e.g., local wind forcing), the presence of this forcing does not corrupt the estimate of H, so long as the additional forcing is uncorrelated with the local dynamic height fluctuations (as is likely to be the case for wind forcing).

[30] Using the measured v from the current meters at 50 and 110 m depths and the dynamic height at 50 m relative to 110 m from the period 2 September 1997 to 14 September

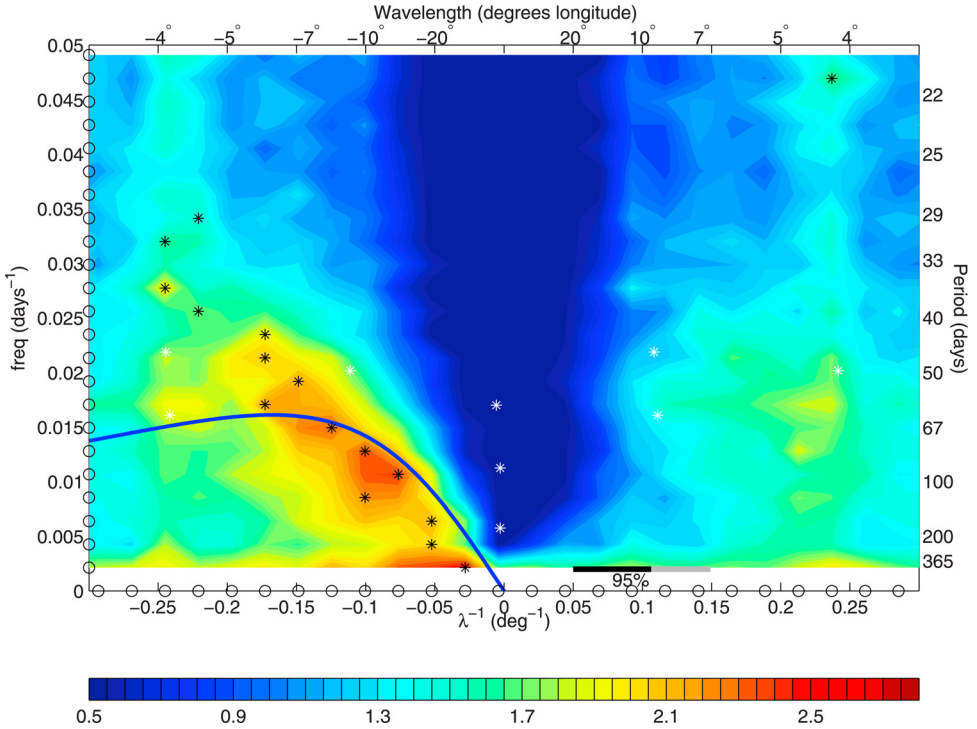

Figure 14. Wave number-frequency spectrum of SSH zonal slope along 10.25°N from 1993 to 2001. For reference, the Rossby wave dispersion relation is shown for free, first baroclinic mode Rossby waves computed with the zonal mean value of the deformation radius given by *Chelton et al.* [1998] and a meridional wave number of zero (blue line). The color bar has a $\log_{10}$ scale with units of mm^2/deg^2/cpd/deg, and the width of the 95% confidence interval (with respect to the color scale) is indicated by a black line for an optimistic estimate of the degrees of freedom. For the more conservative estimate of degrees of freedom described in the text, the additional uncertainty is indicated by the grey line. The black circles indicate the discrete values of frequency and wave number for the estimate. The black asterisks mark the peak power in each frequency band, and the white asterisks mark tidal alias wave numbers and frequencies from *Schlax and Chelton* [1994].

1998, we computed the coherence amplitude and phase using a discrete Fourier transform method. After averaging the spectral estimates across three adjacent (nonoverlapping) frequency bands, the most energetic low-frequency band for both v and η_t was centered on 0.0186 cpd (1/54 d^{-1}), representing the variability in the 44- to 69-day period band. Within this frequency band, the coherence amplitude of 0.95 exceeded the level of no significance at 95% confidence (which is about 0.90), and the phase angle was −11.3° (i.e., η_t leading v). The estimated phase speed is westward at 11.3 ± 5.5 cm/s, where the error bars express 90% confidence limits for the estimates as given by *Bendat and Piersol* [1971]. (The 95% confidence intervals for phase speed are ±7.0 cm/s.) This calculation confirms the notion that the intraseasonal fluctuations in temperature and dynamic height observed at the mooring are associated with westward propagating motions, and the estimated phase speed is consistent with the phase speed estimate made by inspection of Figure 9. The estimate is comparable to the phase speed estimates near 10°N made by *Perigaud* [1990] (14 cm/s) and *Ballestero and Coen* [2004] (12.6 cm/s), but it is somewhat less than the phase speed estimates reported by *Giese et al.* [1994] (17 cm/s).

[31] The zonal wavelength of the intraseasonal variability observed at the mooring site can be estimated using the phase speed estimate by noting that $c_p = \lambda\sigma$, where λ is the zonal wavelength and σ is the frequency. Thus the estimated zonal wavelength for the 44- to 69-day variability at the mooring site is 526 ± 252 km (4.8 ± 2.3° longitude), where the error bars again express 90% confidence limits (95% confidence intervals are ±3.0°). Again, this estimate is consistent with the wavelength estimated by inspection of Figure 9. The estimate also overlaps with the zonal wavelength for energetic intraseasonal variability of 630–950 km identified by *Perigaud* [1990], though the period band considered here (44–69 days) represents only a subset of the period band of 50–90 days considered by Perigaud. While the study of intraseasonal variability by *Giese et al.* [1994] did not offer a quantitative estimate of zonal scale, inspection of their Figure 6 suggests a zonal scale of 1100–1600 km (i.e., 10–15°). Note that *Giese et al.* [1994] examined TOPEX data that were averaged into 3° longitude bins, so that we should expect variability at scales less than about 12° to be poorly represented in their analysis.

[32] We attempted to estimate the meridional wavelength of the 1998 intraseasonal variability at the mooring site by the same method. However, we could not obtain statistically significant intraseasonal coherence between zonal velocity and the dynamic height or its time derivative.

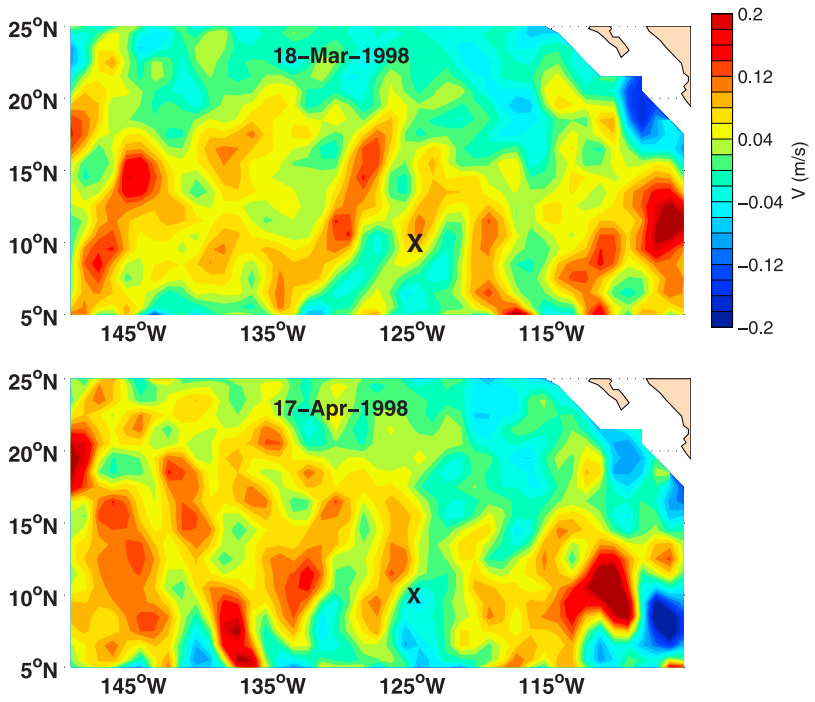

Figure 15. Surface meridional velocity in the *Bonjean and Lagerloef* [2002] surface current analysis during (top) March and (bottom) April of 1998. The mooring location is marked by a cross at 10°N, 125°W. The wave observed by moored instrumentation in the spring of 1998 is visible at the mooring, and it propagates about half a cycle in the 30 days between the two images.

Given the zonal wave number, another way of estimating the meridional wave number is to compute the transfer function between zonal and meridional velocity, which yields an estimate of the ratio of meridional to zonal wave numbers. However, zonal and meridional velocities were also incoherent at intraseasonal frequencies. There are a number of reasons why zonal velocity might be incoherent with dynamic height and meridional velocity, but the most plausible reasons are that either (1) the meridional wave number varies significantly through time while the zonal wave number does not or (2) the meridional wave number is much smaller than the zonal wave number, yielding a wave-induced zonal velocity signal that is small. The second possibility is more likely given the lack of a clear zonal velocity signal corresponding to the 2-month signal in meridional velocity (e.g., Figure 5). Although the signal is not well resolved in the gridded TOPEX/Poseidon data, a signal matching the zonal wavelength estimated at the mooring and seen in the SST data is intermittently visible in the SSH data and in the *Bonjean and Lagerloef* [2002] surface current analysis, derived largely from gridded TOPEX/Poseidon data. The phase of this meridional velocity signal (Figure 15) matches that observed at the mooring site, but it is noisier and weaker than the observed velocity signal (compare to Figure 4). Both of these shortcomings probably result from poor resolution of the approximately 5° wavelength signal in the 1° gridded data used by *Bonjean and Lagerloef* [2002] and from poor resolution of the signal by the TOPEX/Poseidon flight track itself. Despite these shortcomings, the surface current analysis suggests that the meridional wavelength of the signal observed at the mooring site is perhaps 2–3 times as large as the zonal wavelength, and this helps to explain the incoherency of zonal velocity with dynamic height and meridional velocity at intraseasonal periods.

6. Discussion

[33] We have worked to develop a more complete characterization of the intraseasonal variability in dynamic height and currents near 10°N in the eastern tropical Pacific Ocean. For this characterization, we have drawn on in situ observations, satellite altimetry, and satellite SST. The 17-month time series of in situ current and dynamic height observations at 10°N, 125°W reveal the presence of energetic intraseasonal variability. Longitude-time diagrams of SST and zonal slope of SSH anomaly and the wave number-frequency spectrum of sea surface zonal slope indicate that most of the variance in the intraseasonal band is associated with westward propagating motions having a zonal wavelength of 5–15° of longitude. The zonal scales of these motions ($\lambda/2\pi$) are comparable to the first baroclinic deformation radius ($L_D \approx 1°$ [*Chelton et al.*, 1998]). Analysis of the in situ current and dynamic height data suggests that the signal observed at the mooring during the spring of 1998 was due to a westward propagating signal with a phase speed of about 11 cm/s and a zonal wavelength of about 5° longitude. The amplitude of this intraseasonal variability has a strong annual cycle and tends to be largest in April.

[34] In this section we first discuss the interpretation of the intraseasonal variability near 10°N as westward propa-

gating Rossby waves and then discuss the mechanisms that may generate the intraseasonal signal.

6.1. Observed Intraseasonal Variability and the Rossby Wave Dispersion Relation

[35] The wave number-frequency spectrum of observed sea surface zonal slope (Figure 14) shows energy at 40- to 60-day periods propagating westward at 8–15 cm/s. Overlaid on the spectrum is the dispersion curve for a free, first-mode baroclinic Rossby wave with a meridional wave number of zero, where mean flow effects are ignored. The peak of this curve, which occurs at a wavelength of $2\pi L_D \approx 6°$ and a frequency of $\sigma_{\max} = \frac{\beta L_D}{4\pi}$, represents the maximum theoretical frequency at which nonequatorially trapped baroclinic quasi-geostrophic signals can exist in the absence of Doppler shifting by the mean flow [cf. *Gill*, 1982]. Here, L_D is the Rossby deformation radius, which is taken to be the zonal mean of the values given by *Chelton et al.* [1998]. There are a few reasonable explanations that can account for the presence of significant energy in sea surface zonal slope at frequencies higher than this curve. Perhaps the most likely explanation is that, at this latitude of mean westward flow, first baroclinic mode signals are Doppler shifted by the NEC. Another possible explanation is that the energy at these frequencies and wave numbers is due to equatorial Rossby waves that are weakly trapped (i.e., meridional mode numbers greater than 2). *Perigaud* [1990] showed that the intraseasonal variability seen near 10°N is neither symmetric nor antisymmetric about the equator, so this possibility is not likely. Barotropic motions can exist at much higher frequencies because the barotropic deformation radius is much larger. It is conceivable that barotropic motions contribute to the variance observed at these wave numbers and frequencies. However, given that the energy in SSH anomaly is largely associated with the first baroclinic mode [*Wunsch*, 1997] and that the intraseasonal variability is associated with baroclinic disturbances (e.g., Figure 4), it seems unlikely that barotropic motions are responsible.

[36] We now explore the possibility that the observed dispersion characteristics of the intraseasonal variability near 10°N are due to Doppler shifting by the mean zonal flow. In the presence of a spatially uniform steady zonal flow, U, the Rossby wave dispersion relation for a 1.5 layer flow is given by [e.g., *Pedlosky*, 1987, p. 109]

$$\omega = \frac{kU(k^2 + l^2) - \beta k}{k^2 + l^2 + L_D^{-2}}, \tag{5}$$

where k and l are the zonal and meridional wave numbers. A more accurate dispersion relation can be formulated by linearizing the governing equations about a meridionally varying zonal flow [e.g., *Chelton et al.*, 2003], but because the most energetic intraseasonal signals are confined to a fairly narrow latitude band (10–13°N [*Perigaud*, 1990; *Giese et al.*, 1994]) and the flow is similar over this latitude band, we expect that equation (5) will provide a reasonable approximation to the dispersion curve of the energetic intraseasonal variability in the presence of the westward NEC.

[37] Equation (5) is the primary theoretical basis for the so-called "non-Doppler shift" of long Rossby waves [e.g., *Kessler*, 1990]. Long Rossby waves ($k \approx 0$ and $l \approx 0$) are relatively insensitive to the mean flow because the first term in the numerator goes to zero with k and l more rapidly than the second term; in contrast, short Rossby waves are susceptible to substantial Doppler shifting by the mean flow. The definition of a long wave can be based on the criterion that the wave travels westward though a quiescent background at a speed that is some fraction, say 90%, of the speed of a wave with infinite wavelength. At 10°N in the eastern Pacific, the tilted eastern boundary prohibits waves of infinite meridional scales. Waves here with comparable meridional and zonal scales (and $L_D = 93$ km) would need a zonal wavelength of at least 23° longitude to be considered long and be insensitive to Doppler shifting. If we took $l = 0$ despite the tilted eastern boundary, a wavelength of 16° longitude would be considered long. In the western Pacific, with its lack of strongly tilted boundaries (but larger L_D), a zonal wavelength of 20° longitude would be considered long. Even these long waves will be Doppler shifted if the zonal flow is strong enough; it is the ratio of $U(k^2 + l^2)$ to β that determines whether the non-Doppler shift principle holds. For example, a wave on 10°N in the eastern Pacific travelling in a 30 cm/s westward current with $l = 0$ and a zonal wavelength of 16° longitude will have a phase speed that is about 17% faster than it would in a quiescent ocean.

[38] Although the result is qualitatively similar for a broad range of values of U, choosing the value of U is not trivial. There is significant zonal and temporal variation in the NEC and in the energetic intraseasonal variability, and, even without this variability, choice of an appropriate upper layer zonal flow is not necessarily straightforward [e.g., *Chelton et al.*, 2003]. One might expect the appropriate value of U to be the mean U over the season and region in which the energetic intraseasonal variability is observed. In order to choose an appropriate value for U, we consulted the *Bonjean and Lagerloef* [2002] tropical Pacific surface current analysis for 1993–2004, which provides a good representation of the zonal currents observed at the mooring site. We constructed a monthly mean climatological current field from the *Bonjean and Lagerloef* [2002] currents to consider the seasonal and spatial evolution of the zonal surface currents.

[39] Examination of the spatial structure of the zonal currents suggests that the low-frequency zonal currents observed at the mooring site are not representative of the zonal mean currents or of the zonal currents to the east of the mooring site, where the intraseasonal variability in SSH is greatest. For this reason, we chose a value of U based on the *Bonjean and Lagerloef* [2002] zonal currents, rather than using the zonal currents observed at the mooring. The zonal and temporal mean value of the zonal current along 10.25°N is about −12 cm/s on 88°W–140°E (used for the spectral calculation) and is about −11 cm/s on 88–115°W (the region of strongest variability). To explore the potential role of Doppler shifting by the zonal flow in the observed dispersion curve of the intraseasonal variability, we will use $U = -11$ cm/s. There is considerable uncertainty in the appropriate choice of a vertical averaging interval for U, and without a much more detailed analysis [e.g., *Chelton et al.*, 2003] the choice of U is somewhat arbitrary. Similar ambiguities are involved in choosing a value of the deformation radius. For consistency with the chosen zonal

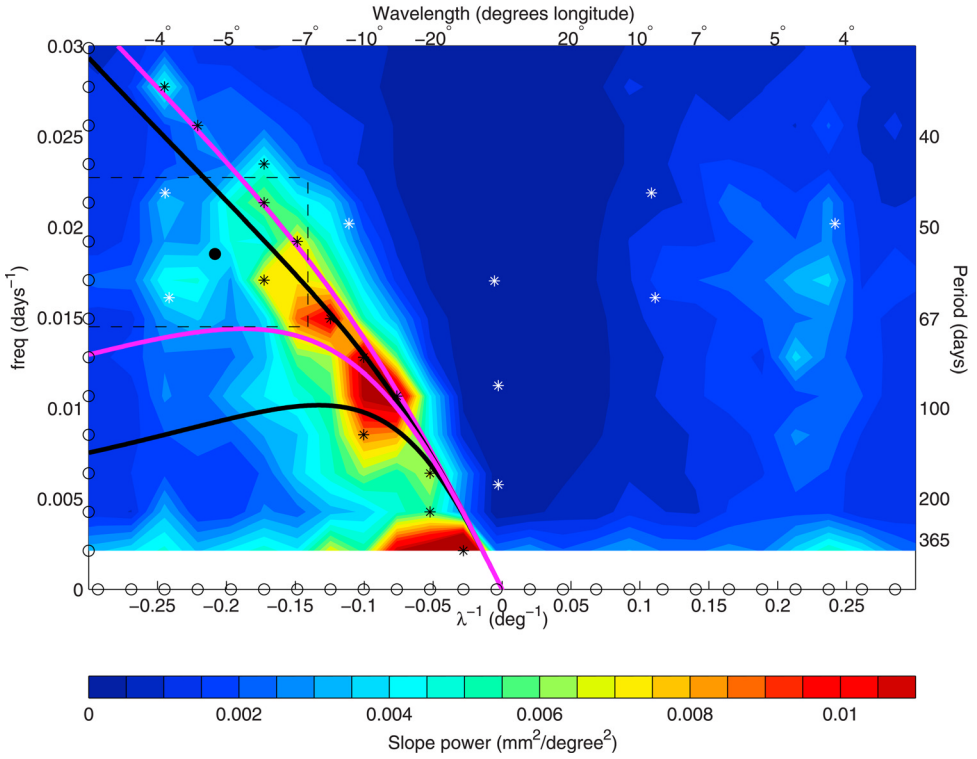

Figure 16. Variance-preserving spectrum of TOPEX/Poseidon zonal sea surface slope in units of mm^2/degree^2 at 10.25°N. Dispersion curves (equation (5)) are shown for $l = 0$ (pink) and $l = k$ (black) with a mean zonal flow of −11 cm/s (top curve) and without mean flow (bottom curve). Black asterisks mark peaks of spectral density at each frequency, white asterisks mark known TOPEX tidal aliases, and the solid black circle marks the wave number and frequency estimated for the wave observed at the mooring. The dashed line marks the 90% confidence interval and frequency band for the mooring estimate.

current, we will take $L_D = 93$ km, the zonal mean over 88–115°W of the climatological first baroclinic deformation radius given by *Chelton et al.* [1998] at 10.25°N. Because of the myriad uncertainties involved in choosing parameters for the dispersion curves, the resulting curves are mainly useful for qualitative understanding of the effect of the NEC on the observed dispersion characteristics. The Doppler shifted dispersion curves are not overly sensitive to the value of U. Changing the mean flow by a few cm/s yields dispersion curves that are quite similar, and the curves for values of U ranging from −6 to −20 cm/s share qualitative similarities.

[40] Figure 16 shows the variance-preserving wave number-frequency power spectrum of sea surface zonal slope. When plotted in this form, it is clear that the variance of sea surface zonal slope at periods less than annual is dominated by 50- to 100-day variability. It is also noteworthy that the M_2 tidal alias with about a 4° westward wavelength and 62-day period [*Schlax and Chelton*, 1994] contributes appreciably to the variance of the zonal slope, though the alias certainly does not dominate the variance. Four dispersion curves for free, first baroclinic mode Rossby waves, with meridional wave numbers ranging from $l = 0$ to $l = k$ and zonal mean flows ranging from zero to −11 cm/s are shown. Given that most of the power in sea surface zonal slope lies near the Doppler shifted dispersion curves, the most energetic motions in sea surface zonal slope (and by extension, the surface meridional velocity) can be interpreted as first baroclinic mode Rossby waves propagating in the westward flowing NEC. Notice that the effect of the Doppler shifting is to make the variability nearly nondispersive and reduce the difference between waves of finite and infinite meridional scale. The wave number and frequency estimated for the velocity signal at the mooring is also indicated; this estimate overlaps the range of frequencies and wave numbers that dominate the variance of sea surface zonal slope.

[41] We suggest that the observed dispersion characteristics of the variability on 10°N can be interpreted as being due to linear Rossby waves in a mean westward flow. This may be an oversimplification, not only because the space-time variability of the westward flow and the deformation radius limits the useful application of equation (5) but also because the strong eddies observed in the eastern Pacific warm pool are likely to be nonlinear. Different nonlinear models of these eddies have been discussed by *Hansen and Maul* [1991] and Yamagata and coinvestigators [*Matsura and Yamagata*, 1982; *Yamagata et al.*, 1990; *Umatani and Yamagata*, 1991]. These models suggest that the eddies should travel slightly faster than the long Rossby wave speed, consistent with other models of nonlinear eddies [e.g., *McWilliams and Flierl*, 1979]. However, the quasi-geostrophic model discussed by *McWilliams and Flierl* [1979] suggests that the eddy speed is constrained by the

linear wavefield in the surrounding fluid, and perhaps this contributes to the wave-like nature of the observed dispersion characteristics.

6.2. Potential Generation Mechanisms

[42] A variety of generating mechanisms for the intraseasonal variability have been proposed in the literature, but no consensus has been reached. The eastern tropical North Pacific is a region of strong wind forcing, annual variability, zonal currents, and a complex mean circulation. More than one of the proposed mechanisms may be involved in setting the properties of the observed intraseasonal variability. *Perigaud* [1990] hypothesized that the intraseasonal variability near 10°N is generated by barotropic instability associated with the NEC/NECC shear, in a manner analogous to the generation of tropical instability waves farther south. However, Perigaud noted that the shear strength along 12°N does not coincide well in space and time with the observed wave growth. *Philander* [1976] suggested that the NEC may be baroclinically unstable; based on a calculation with an idealized two-layer model, he suggested that the resulting waves would have a period of 30 days, a wavelength of 7° longitude, and an *e*-folding time of at least 60 days.

[43] *Yamagata et al.* [1990] showed that sufficiently strong, steady forcing of potential vorticity can generate a sequence of propagating anticyclonic eddies for parameters appropriate to the strong wind stress curl signal associated with the passage of winds through the Central American mountain gaps of Tehuantepec and Papagayo. *Umatani and Yamagata* [1991] appealed to this theory to explain sequential eddies emanating from the Gulf of Tehuantepec in a high-resolution numerical model forced with monthly mean climatological winds. A variant of this idea was proposed by *Giese et al.* [1994], who argued, based on the relative timing of 7 wind events and 5 visible eddies over a 17-month period, that fluctuations in the mountain gap winds may force the intraseasonal eddies. *McCreary et al.* [1989] employed analytical and numerical models to examine eddy generation by the mountain gap winds, and found that a cyclonic and anticyclonic eddy pair develops rapidly in response to the mountain gap winds, but by the time the eddy pair begins to detach from the coast (about 10 days after starting to form) the anticyclonic eddy is much stronger than the cyclonic eddy. Another interesting result of the McCreary et al. analysis is that the anticyclonic eddies emanating from Tehuantepec weaken and broaden as they move away from the coast, whereas the ones from Papagayo do not.

[44] Another possible source of intraseasonal variability in the eastern tropical Pacific is the strong intraseasonal coastal sea level variability associated with baroclinic Kelvin waves propagating poleward along the west coast of the Americas [*Spillane et al.*, 1987]. This variability is believed to result from equatorial Kelvin waves forced by intraseasonal variability in the large-scale zonal winds [*Enfield*, 1987; *Kessler et al.*, 1995; *Zang et al.*, 2002]. The equatorial intraseasonal Kelvin waves have largest amplitude in the boreal fall and winter at 140°W [*Kessler et al.*, 1995]. The amplitude of the coastal sea level and thermocline depth variability is expected to increase as the wave propagates northward from the equator to regions with a smaller deformation radius [*Moore and Philander*, 1977]. The observations of *Spillane et al.* [1987] show peak intraseasonal RMS sea level amplitudes between about 7°N and the Gulf of California of a few centimeters. This intraseasonal coastal sea level and thermocline depth variability may radiate intraseasonal Rossby waves to the west.

[45] *Hansen and Maul* [1991] argued that propagating anticyclonic circulations observed with drifters in the region are caused by conservation of potential vorticity as the NECC collides with the eastern boundary (the retroflection hypothesis). In this hypothesis, water that has travelled eastward in the NECC at a latitude between 5 and 8°N is moved northward along the eastern boundary to about 11°N where the water must take on anticyclonic relative vorticity to conserve potential vorticity. The resulting anticyclonic eddy then propagates westward under the influence of β. At its core, this hypothesis involves only potential vorticity conservation and the notion that the water near 10°N had come from the NECC. This hypothesis is somewhat different from the other three in that it offers only a diagnostic relationship between the eddies and their initial position and potential vorticity, rather than specifying a clear causal chain of events. Put another way, the eddies and the retroflection may be seen as part of a single process, and this process needs explanation; perhaps it would be due to some instability of the NECC or northward advection around the shoreward side of the Costa Rica Dome. It is also unclear to what extent potential vorticity is conserved in the presence of the strong vorticity forcing by the mountain gap winds [*Kessler*, 2002; *Chelton et al.*, 2004] and the vorticity homogenization that may occur at the eastern boundary. The NECC retroflection hypothesis may very well be correct, but, if it is, further work will be required to explain the process that causes the retroflection and the eddies.

[46] Determination of the generation mechanism(s) for the eastern tropical Pacific 50- to 100-day variability along 10°N is beyond the scope of this paper, but we tested the various hypotheses to the extent allowed by our results. Our analysis suggests that the 50- to 100-day variability near 10°N has the following characteristics: (1) The signal is strongest between 120°W and the eastern boundary, but the largest amplitude does not necessarily occur at the eastern boundary. (2) The signal amplitude is annually modulated, with peak amplitudes occurring around April in the region of strongest variability. (3) The signal is associated with zonal wavelengths of 5–15° and westward phase speeds of 10–17 cm/s. (4) The 50- to 100-day SSH amplitude along 10°N increases rapidly over a broad range of longitudes.

[47] This last point may provide an important clue about the generation mechanism for the intraseasonal variability. The wave number-frequency spectrum of sea surface slope suggests that the intraseasonal variability propagates westward in a manner consistent with expectations for first baroclinic mode, free Rossby waves. However, the nearly simultaneous appearance of power on such a broad range of longitudes during the boreal spring would require an unrealistically large westward group speed in order for the energy to have travelled directly westward from the eastern boundary. Moreover, there are no years (with the possible

exception of 1998) where the 50- to 100-day amplitude present at, say, 110°W can be observed to have propagated directly westward from the eastern boundary (Figure 11). This may indicate that the signal originates or grows in the ocean interior, perhaps as a result of instability of the zonal equatorial currents as hypothesized by *Philander* [1976] (baroclinic instability) or *Perigaud* [1990] (barotropic instability). While this line of reasoning suggests that the signal may originate in the ocean interior, it does not rule out the possibility that the 50- to 100-day power was generated near the eastern boundary at another latitude before propagating southwestward to appear offshore at 10°N. We examine this possibility below.

[48] Some insight into the importance of intraseasonal variations in winds can be gained by examination of the output of realistic numerical models that are forced by monthly mean climatological winds. We examined intraseasonal variability in a high-resolution ocean general circulation model (GCM), forced by monthly mean *Hellerman and Rosenstein* [1983] climatological winds, which shows energetic intraseasonal variability near 10°N with frequencies and zonal scales similar to what is observed. This model simulation was carried out by *Jochum and Murtugudde* [2004] for examination of tropical instability waves in the Pacific.

[49] The modeled meridional velocity at the mooring location (not shown) is qualitatively similar to the meridional velocity record observed at the mooring (Figure 4), in that the record is dominated by intraseasonal fluctuations that are more energetic above the pycnocline, and the amplitude and seasonal cycle of the intraseasonal current fluctuations are similar to what is observed. In addition, the wave number-frequency spectrum of the modeled meridional velocity is similar to that of the zonal slope of observed SSH, with both spectra showing elevated variance at similar wave numbers in the intraseasonal band. Comparison of longitude-time plots of the model's meridional velocity to the observed zonal slope of SSH reveals some qualitative differences, though. One notable qualitative difference is in the longitude of maximum amplitude; in the observations, the intraseasonal signal in sea surface slope has a maximum near 100–115°W, whereas the signal in the model meridional velocity has a maximum amplitude near 130°W and a weaker local maximum near 100°W. The intraseasonal currents in the model are different each year and the monthly mean climatological winds used to force the model have little energy at intraseasonal frequencies, so it seems unlikely that the intraseasonal variability in the model is due to direct wind forcing at intraseasonal frequencies as hypothesized by *Giese et al.* [1994] for the observed intraseasonal variability. *Umatani and Yamagata* [1991] also found strong intraseasonal variability in a high resolution (0.25°) ocean model forced by the same monthly mean winds. They attributed the variability to excitation of successive eddies by the steady supply of potential vorticity at the Gulf of Papgayo via the nonlinear mechanism described by *Yamagata et al.* [1990]. The retroflection hypothesis or instabilities of the zonal equatorial currents might also explain the presence of intraseasonal variability in the models, but direct forcing by intraseasonal wind variations does not seem to be fundamental to the existence of the intraseasonal velocity variability.

6.2.1. Baroclinic Instability?

[50] Before relating the results from 10°N to the dynamics of the broader region, we briefly explore the possibility that the variability on 10°N is associated with baroclinic instability of the NEC. *Philander* [1976] employed the *Phillips* [1951] model to show that the NEC may be baroclinically unstable. For a two-layer system with a very small Rossby number, a necessary condition for baroclinic instability of a uniform westward zonal current is

$$U_1 - U_2 < \frac{-\beta g' H_1}{f^2}, \tag{6}$$

where g' is the reduced gravity, H_1 is the thickness of the upper layer, and U_1 and U_2 are the velocities of the upper and lower layers. The deformation radius of the first baroclinic mode is $L_D = \sqrt{g' H_1 H_2}/f\sqrt{H_1 + H_2}$ where H_2 is the lower layer thickness. For $H_1/H_2 \rightarrow 0$ (a reasonable approximation for the eastern tropical Pacific), the necessary condition for baroclinic instability is given approximately by an upper layer flow satisfying

$$U < -\beta L_D^2. \tag{7}$$

(In this limit of an infinitely thick lower layer, $U_2 \rightarrow 0$.) Note that $-\beta L_D^2$ is the speed of phase and energy propagation for long Rossby waves. Using equation (7) and the zonal mean value of the deformation radius given by *Chelton et al.* [1998] for 88–115°W on 10.25°N, we find that this approximate necessary condition for baroclinic instability is met when $U_{\mathrm{crit}} \approx -20$ cm/s. In theory, an eastward zonal current can also be baroclinically unstable, but because the upper layer of the tropical Pacific is much thinner than the lower layer, eastward currents require a much larger flow speed for instability. *Pedlosky and Thomson* [2003] have recently shown that time-dependent zonal flows can become baroclinically unstable at even lower speeds than implied by the steady model.

[51] Clearly, the two-layer model is a highly idealized approximation to the real ocean and the zonal flow in the region has considerable spatial and temporal variability, so the value of U_{crit} given here is not likely to be quantitatively accurate. *Gill et al.* [1974] compared baroclinic instability in the two-layer model to that in a continuously stratified fluid and discussed strengths and shortcomings of the two-layer model. Serious shortcomings of the two-layer model are its neglect of near surface horizontal density gradients, which can dramatically affect stability properties, and the poorly constrained choice of appropriate values of g', H_1, and H_2. When $H_1/H_2 \rightarrow 0$, the latter difficulty is somewhat alleviated because we only need to specify the first baroclinic deformation radius, which is well constrained by available data. Neglect of horizontal density variations is certainly an issue, but we can at least note that a negative meridional temperature gradient (i.e., warmer water to the south) tends to stabilize a westward current, whereas a positive temperature gradient tends to destabilize the current. During the season of active intraseasonal variability (as well as in the long term mean, e.g., Figure 1), the meridional surface temperature gradient is positive on 10°N in the eastern Pacific because the peak SSTs of the eastern Pacific warm

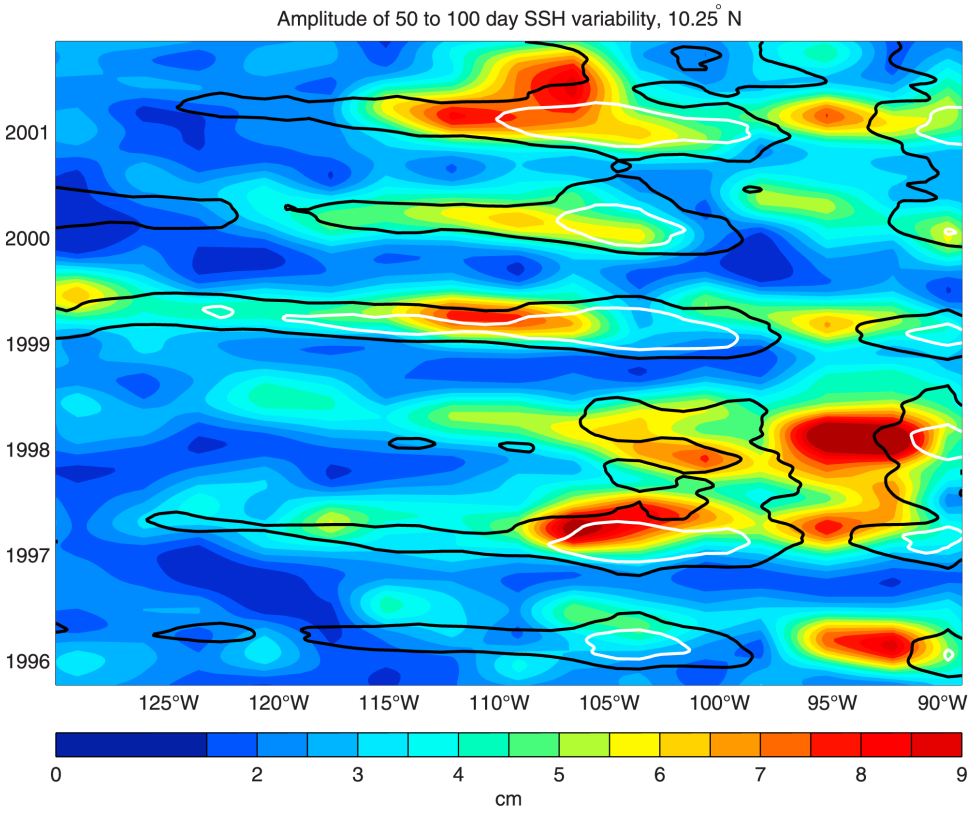

Figure 17. Amplitude of 50- to 100-day SSH signal along 10°N (color contours). Contours of low-frequency (125-day running mean) zonal velocity are shown at −15 cm/s (black contours) and −25 cm/s (white contours) and indicate the possibility of baroclinic instability (equation (7)).

pool are to the north. In the central and western Pacific, the surface temperature gradient is generally negative, so we expect this region to be more stable than the two-layer model would suggest.

[52] We have attempted to determine whether there is a link between the westward zonal current and the growth of 50- to 100-day oscillations near 10°N in the eastern tropical Pacific by reexamining the amplitude of 50- to 100-day SSH variability in the eastern tropical Pacific during 1996–2001 in the context provided by the *Bonjean and Lagerloef* [2002] surface current estimates. Figure 17 shows the amplitude of 50- to 100-day SSH variability in the eastern tropical Pacific during 1996–2001. The 125-day running mean westward zonal current from the *Bonjean and Lagerloef* [2002] surface current analysis is also indicated. As is often noted [e.g., *Pedlosky*, 1987, p. 491], the observed zonal flow is not necessarily a good measure of the background zonal flow that would exist in the absence of instabilities because the observed flow is altered by the presence of instabilities. Nevertheless, the space-time correspondence of strength of the westward flow with the amplitude of 50- to 100-day variability is remarkable. Episodes of intense 50- to 100-day SSH variability are typically preceded by an increase of westward flow speeds associated with the normal seasonal cycle of the NEC. In addition, the westward flow often decreases as the 50- to 100-day oscillations grow, suggesting that the 50- to 100-day oscillations may be drawing energy from the large-scale zonal current. The GCM output discussed earlier exhibits a similar relationship of westward flow speed and 50- to 100-day variability. These facts suggest that the intraseasonal variability and its annual cycle are influenced by baroclinic instability of the NEC in the eastern part of the basin.

[53] While baroclinic instability does seem to be a plausible explanation of some the observed properties of the intraseasonal variability, some of the other hypotheses may be equally plausible. It is not obvious that the baroclinic instability hypothesis can explain the often-noted tendency for anticyclonic eddies in the region [e.g., *Hansen and Maul*, 1991; *Giese et al.*, 1994], and the space-time correlation of 50- to 100-day amplitude with zonal flow speeds meeting the approximate instability condition may be a mere coincidence. Most properties of the eastern tropical Pacific in the region have a strong annual signal, so correlation of two quantities in the region at annual periods is not especially strong evidence of a direct causal relation. Anticyclonic eddies have been observed to propagate southwest from the Gulf of Tehuantepec at about 13°N and either cross or travel along 10°N on 100–115°W [e.g., *Giese et al.*, 1994]. This could explain the enhanced intraseasonal variability in the region, and the coherence with the zonal flow might be explained as a rectification of the velocity of the eddies (though, if this were the case, we would expect peak eddy activity to occur at the same time as peak low-frequency zonal flow). Both the coastal wind forcing and retroflection hypotheses can readily explain the tendency for anticyclonic eddies. Without the full context in

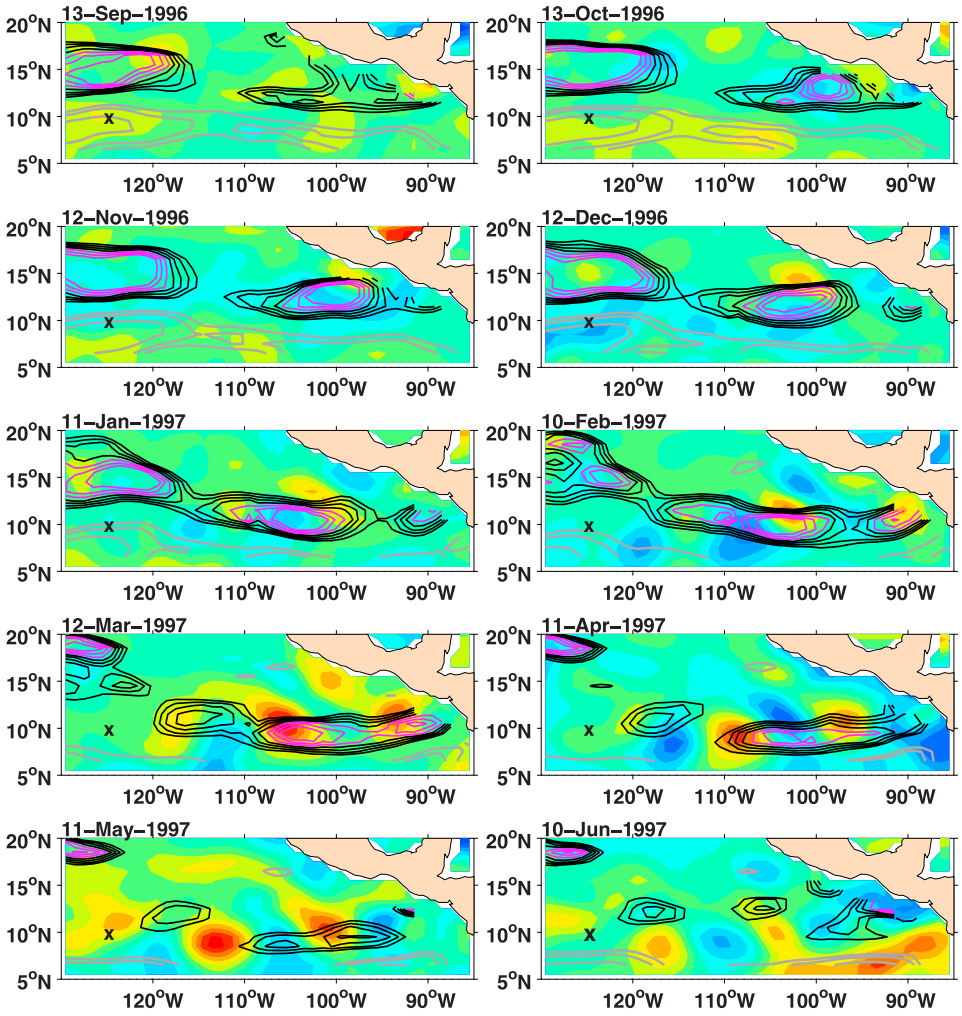

Figure 18. The 50- to 100-day SSH anomaly (filled color contours). The contour interval is 1 cm, and the color scale spans ±8 cm. Eastward flow speeds are contoured (grey lines) at speeds of 10, 15, and 25 cm/s. $U/\beta L_D^2$ (equation (7)) is contoured at values of 0.4, 0.5, 0.6, and 0.7 (black lines) and at values of 0.8, 0.9, and 1 (pink lines).

latitude, longitude, and time, the results from 10°N are difficult to interpret, so we now briefly consider the evolution of the variability in latitude and longitude.

6.2.2. Examination of the Variability in its Dynamical Context

[54] We examined sequential images of 50- to 100-day band-passed SSH (from the 1° gridded WOCE TOPEX/Poseidon product) from the 1994–2002 seasons and present sequential images for the 1997 and 1999 seasons here (Figures 18 and 19). We take a "season" to encompass the periods before, during, and after peak 50- to 100-day variability (i.e., roughly October–June). The choice of years was motivated by the following factors. With the exception of the 1998 season, which involved a rapid transition from a strong El Niño to a strong La Niña, the different seasons were qualitatively similar. We chose the 1997 season because it includes some eddies that passed the mooring site during the early part of the mooring deployment (May–August 1997), and we excluded the 1998 season because the adjustment from El Niño to La Niña makes the imagery difficult to interpret (e.g., Figure 17). In addition, the waves observed at the mooring site during the spring of 1998 are not well resolved in the 1° gridded SSH data, so little insight into these waves is gained through inspection of sequential images. We chose the 1999 season because Figure 17 indicates that there was a broad region of the NEC along 10°N that was potentially baroclinically unstable during this time.

[55] We also estimated the surface geostrophic flow using the 1° gridded WOCE TOPEX/Poseidon product and the mean dynamic height relative to 1000 m from *Levitus et al.* [1997] following *Bonjean and Lagerloef* [2002]. We chose to compute the geostrophic flow in this way because the *Bonjean and Lagerloef* [2002] currents include an Ekman flow with a westward component near 10°N due to the northeasterly trade winds. Excluding the Ekman flow, which does not contribute directly to instability, allows a more rigorous test of the baroclinic instability hypothesis. The currents used here are qualitatively similar to the *Bonjean and Lagerloef* [2002] currents, but tend to be weaker. To allow examination of the possibility that baroclinic instability influences the evolution of 50- to 100-day

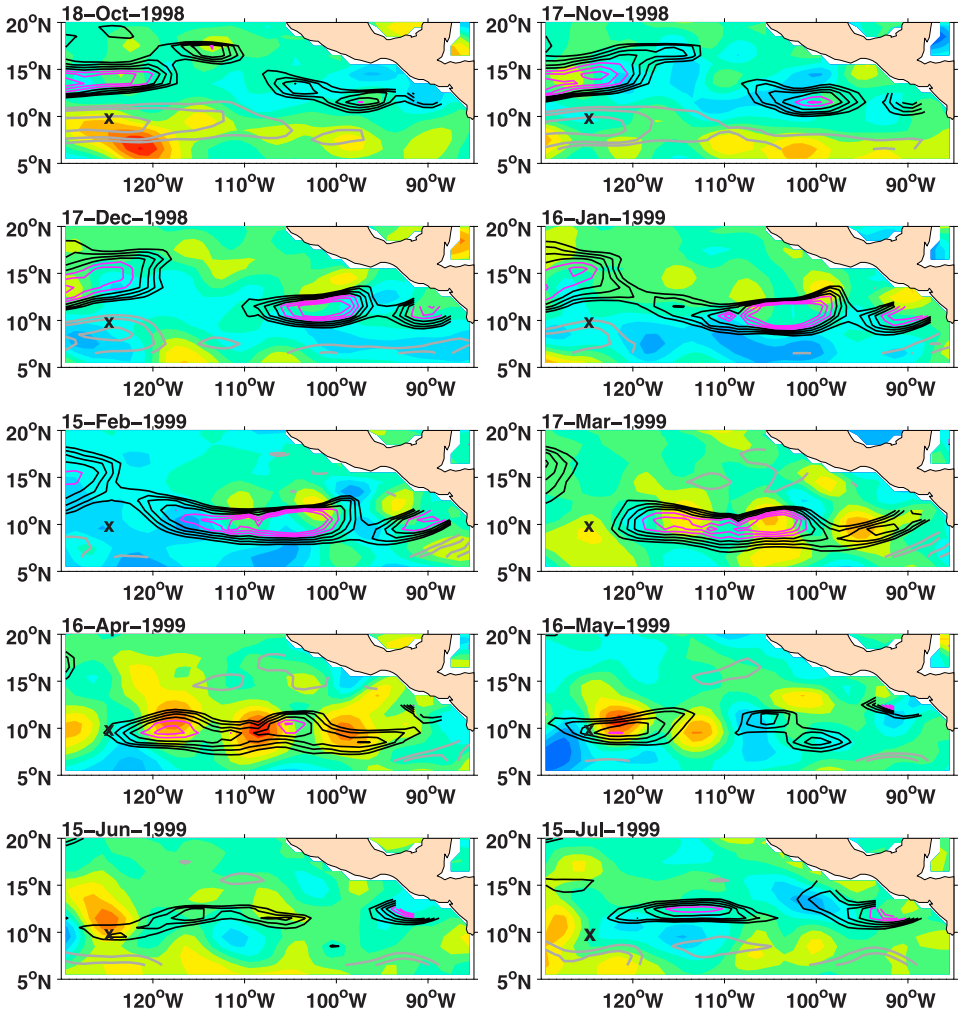

Figure 19. The 50- to 100-day SSH anomaly (filled color contours). The contour interval is 1 cm and the color scale spans ±8 cm. Eastward flow speeds are contoured (grey lines) at speeds of 10, 15, and 25 cm/s. $U/\beta L_D^2$ (equation (7)) is contoured at values of 0.4, 0.5, 0.6, and 0.7 (black lines) and at values of 0.8, 0.9, and 1 (pink lines).

SSH amplitude, contours of $U/\beta L_D^2$ are indicated for westward currents. We also overlaid contours of the NECC zonal current speed in Figures 18 and 19 to facilitate evaluation of the retroflection hypothesis. All zonal currents were low-pass filtered with a 100-day cutoff. To strike a balance between covering a broad time period and displaying a manageable number of images, we chose to show images at 30-day intervals. In most cases, this still allows eddies and other 50- to 100-day SSH anomalies to be tracked through sequential images.

[56] Each year, both positive and negative 50- to 100-day SSH anomalies emanate from near the gulfs of Tehuantepec and Papgayo, though the positive anomalies are typically of larger amplitude, consistent with the calculations of *Umatani and Yamagata* [1991] and *McCreary et al.* [1989]. Much of the variability in 50- to 100-day SSH on 10°N appears to be related to anticyclonic eddies propagating southwestward from the Gulf of Tehuantepec, consistent with the observations of *Giese et al.* [1994]. The NECC impinges on the eastern boundary around December/January, though our computation of the geostrophic flow extends to within only about 2° of the coast. For a northward flow speed of 20 cm/s, it would take about 15 days for water to travel from 7°N to 11°N; during both of the seasons shown, anticyclonic eddies appear to form near 11°N within about a month of the NECC retroflection. However, the time of retroflection from the images is subject to considerable uncertainty, and it is not possible to determine whether the anticyclonic eddy formation is due to retroflection or wind forcing without further analysis. It is difficult to reliably identify Rossby waves radiating from intraseasonal Kelvin waves at the coast by inspection of the SSH imagery. Still, there are times (e.g., May and July frames of 1999 and other times not shown) when the images give the impression of large-scale, coherent coastal sea level variability radiating to the west.

[57] The eastern branch of the NEC (east of about 120°W; as indicated by contours of $U/\beta L_D^2$) is typically weaker and farther north during September–December than during January–March, consistent with *Wyrtki*'s [1975] analysis

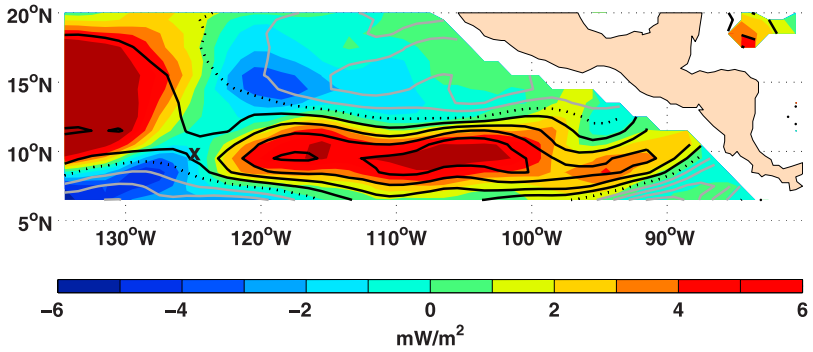

Figure 20. Mean work by the wind on the seasonally varying geostrophic flow ($\langle \boldsymbol{\tau} \cdot \mathbf{u}_g^{\text{slow}} \rangle$) over the period 1 January to 15 June 1999. Contours of the mean zonal flow during the period are overlaid at intervals of 4 cm/s; eastward zonal flows are indicated by grey contours, and the zero contour is dashed.

of hydrographic data. (Note that, for a given value of U, $U/\beta L_D^2$ will be larger at higher latitudes because both β and L_D tend to decrease to the north.) Around the time of peak 50- to 100-day amplitude (i.e., roughly March–May), the eastern branch of the NEC weakens considerably, decreasing in speed by a factor of two or more.

[58] The amplitude of the eddies increases as the eddies move away from the coast, reaching maximum amplitudes on 10–12°N between 100–120°W between March and May, consistent with the analysis along 10°N for 1993–2001 in section 4. In this region, systematic growth of eddies occurs almost exclusively while the eddies are in contact with parts of the NEC that meet the criterion for baroclinic instability. The variability appears to become more spatially organized as the NEC reaches peak intensity around January/February, about 2 months before the peak eddy amplitudes are reached. In addition, there are growing eddies that do not appear to have come from the eastern boundary. For example, the eddy that is first identifiable near 12°N, 108°W on 16 January 1999 intensifies, along with the other eddies in contact with the "critical" NEC, and propagates westward past the mooring site during June 1999. Another such example is the eddy forming at 12°N, 111°W on 11 January 1997. The eddies reach peak amplitudes within about 2 months of peak flow speeds in the eastern branch of the NEC, and the NEC weakens as the eddies intensify. By about June, the eastern branch of the NEC almost completely disappears, and the eddies rapidly decay and/or disperse. In most years, the eddies are virtually unidentifiable by July.

[59] The fact that the NEC weakens as the eddies grow suggests that the eddies may be extracting energy from the low-frequency zonal currents. However, a number of other mechanisms could explain the weakening of the NEC. One likely mechanism is direct wind forcing. *Kessler* [2002] showed that the weakening of the climatological NECC near 7°N, 110°W is due to direct wind forcing. One way of determining whether the weakening of the NEC observed between January and June is also due to direct wind forcing is to compute the wind energy input to the geostrophic flow over this time period. If the wind energy input is negative, then the wind works to decrease the energy of the flow and the observed decrease in strength of the NEC could be explained by direct wind forcing. We take the wind work on the geostrophic flow to be given by [*Stern*, 1975; *Fofonoff*, 1981; *Wunsch*, 1998]

$$W = \langle \boldsymbol{\tau} \cdot \mathbf{u}_g \rangle = \langle \boldsymbol{\tau} \cdot \mathbf{u}_g^{\text{slow}} \rangle + \langle \boldsymbol{\tau} \cdot \mathbf{u}_g^{\text{rapid}} \rangle, \tag{8}$$

where the angle brackets denote a time average over January–June and $\boldsymbol{\tau}$ is the wind stress. The second equality follows from a trivial modification to *Wunsch*'s [1998] approach, made to distinguish between the eddies ($\mathbf{u}_g^{\text{rapid}}$, timescales less than 100 days) and the seasonally varying geostrophic flow ($\mathbf{u}_g^{\text{slow}}$, timescales greater than 100 days). Derivation of this expression assumes that the dominant dynamics are geostrophic and Ekman balance (or Sverdrup balance [*Wunsch*, 1998]) which is probably a decent approximation for the annual mean flow [*Kessler*, 2002]. The surface geostrophic flow was computed from TOPEX/Poseidon and mean dynamic height data as described earlier in this section. We utilized the scatterometer wind stress data from the European Space Agency's ERS2 satellite. For 1997 (not shown) and 1999 (Figure 20), the work by the wind on the eastern branch of the NEC is positive with values of a few mW/m^2, comparable to the global average value of wind work on the geostrophic flow estimated by *Wunsch* [1998]. For comparison, the estimated work by the wind on the eddies, averaged over 10–13°N and 95–120°W, is about −0.013 mW/m^2 in 1997 and about 0.013 mW/m^2 in 1999; both values are a few hundred times smaller than the energy input to the seasonally varying geostrophic flow. In retrospect, it is not surprising that the wind work on the NEC should be positive, since the trade winds and the NEC are generally in the same direction. The tendency of the wind to strengthen the NEC near 10°N, 105°W is consistent with *Kessler*'s [2002] interpretation of the mean dynamical balance of the region, in which the downwelling-favorable curl($\boldsymbol{\tau}/f$) signal extending from the Gulf of Tehuantepec strengthens the thermocline trough near this location. Despite the fact that the wind stress acted to increase the energy of the eastern branch of the NEC over the period January–June, the current speed (and energy) decreased dramatically. One plausible explanation for the decrease in strength of the current is energy extraction by the growing eddies, but examination of one term in the energy balance is far short of a complete energy budget. Vertical mixing or horizontal advection of energy by the mean flow

could cause the current to decrease even as the wind works to increase the energy of the current. Still, we can safely infer that direct wind forcing cannot be responsible for the observed decrease in energy of the current.

7. Conclusion

[60] We have examined the characteristics of intraseasonal variability near 10°N in the eastern tropical Pacific using in situ and satellite data. The observations show that both wavelike and eddy-like motions contribute to the intraseasonal variability. We found that the variability is annually modulated, with strongest amplitudes tending to occur around April, but there is also substantial spatial and interannual variability in the intraseasonal signal. Besides being of potential importance for meridional heat transport and air-sea interaction, this variability poses a sampling challenge to those working to study air-sea coupling and other processes in the vicinity of 10°N in the eastern Pacific.

[61] When viewed on a zonal section along 10°N, the amplitude of the intraseasonal variability seems to increase too rapidly to be explained by due westward energy propagation. Some intraseasonal eddies travel southwestward to 10°N from near the Gulf of Tehuantepec, and this can explain part of the rapid increase of intraseasonal variability on 10°N. In addition, some of these eddies appear to intensify after coming into contact with a potentially baroclinically unstable NEC. The wavelike intraseasonal variability observed at the mooring site during the first half of 1998 modified SST by meridional advection along the slowly evolving horizontal surface temperature gradient. The strong eddies observed near the coast are also known to produce strong SST signatures by advection and also by upwelling/downwelling and entrainment during their generation stage [e.g., *McCreary et al.*, 1989].

[62] We now briefly summarize our understanding of the generation mechanism for the intraseasonal variability seen near 10°N in the eastern tropical Pacific. We have shown, as have others [e.g., *Giese et al.*, 1994], that eddies emanate from near the gulfs of Tehuantepec and Papagayo and propagate westward along 10–13°N. Under monthly mean climatological wind forcing, the GCM output of *Jochum and Murtugudde* [2004] and *Umatani and Yamagata* [1991] shows intraseasonal variability near 10°N, which suggests that intraseasonal fluctuations in the mountain gap winds (i.e., the hypothesis of *Giese et al.* [1994]) are not fundamental to the existence of the variability, though the wind fluctuations certainly may play an important role in determining the details of the observed variability. Eddies are generated near the eastern boundary with remarkably high frequency; for example, *Gonzalez-Silvera et al.* [2004] identified 18 eddies being shed from the gulfs of Tehauntepec and Papagayo during the 5-month period of November 1998 to March 1999. It remains unclear how these frequently generated eddies might contribute to intraseasonal variability near 10°N. We have not endeavored to determine whether the intraseasonal eddies observed at the eastern boundary are forced by the wind or are associated with retroflection, though there is substantial evidence for wind forced eddies [e.g., *Stumpf and Legeckis*, 1977; *McCreary et al.*, 1989; *Clarke*, 1988] and the Gulf of Tehuantepec seems rather far from the NECC for retroflection to make sense as a generation mechanism there. Nonetheless, *Ballestero and Coen* [2004] have suggested that their observations near the Gulf of Papagayo are consistent with both interpretations.

[63] Our analysis suggests that the eddies typically strengthen in March–May, well away from the coast and while in contact with a potentially baroclinically unstable NEC. While the eddies grow, the NEC weakens considerably, despite continued energy input from the wind. We have not attempted to determine whether barotropic instability might also contribute to the disturbances. It is worth noting that *Jochum and Malanotte-Rizzoli* [2003] examined variability at similar frequencies and scales in the northern tropical Atlantic of a GCM and concluded that both baroclinic and barotropic instability contributed energy to those disturbances. One interpretation of the existing literature and the observations presented here is that wind forcing (and possibly other mechanisms) generates disturbances that propagate into an unstable NEC. As the disturbances draw energy from the current, the current weakens considerably. When the eastern branch of the NEC stabilizes, the disturbances rapidly decay and disperse, and the stage is set for the next annual cycle. We have not been able to fully evaluate the various hypotheses for the intraseasonal variability here, but the observations suggest that baroclinic instability contributes to the intraseasonal variability.

[64] The eastern Pacific warm pool is of potential importance for weather and climate simulation because of its effect on large-scale weather patterns, and the oceanic intraseasonal variability there is likely to play a role in the warm pool's mean heat balance. The relative roles of wind forcing, NECC retroflection, and instability in generating intraseasonal variability in the region could be studied through analysis of energy conversion terms and potential vorticity in a high-resolution GCM [e.g., *Masina et al.*, 1999; *Jochum and Malanotte-Rizzoli*, 2003]. We hope the recent EPIC experiment [*Raymond et al.*, 2004] and future observational programs will yield further understanding of the complex dynamics and thermodynamics of the region.

[65] **Acknowledgments.** The authors gratefully acknowledge support for the fieldwork under the NOAA Office of Global Programs Pan American Climate Studies program (grants NA66GPO130 and NA96GPO428) and for analysis and publication (grants NA87RJ0445 and NA17RJ1223). This work is done as part of the U.S. CLIVAR program. The mooring observations were collected by the WHOI Upper Ocean Processes group. Steve Anderson played a vital role in planning and executing the mooring program. We gratefully acknowledge Markus Jochum and Raghu Murtugudde for providing the ocean general circulation model fields. Many scientists and students in the Department of Physical Oceanography at WHOI gave J.T.F. valuable feedback during the course of this work. Billy Kessler and an anonymous reviewer provided helpful suggestions. The *Bonjean and Lagerloef* [2002] surface currents were obtained from the NOAA Ocean Surface Current Analyses Real-time (OSCAR) Project Office (http://www.oscar.noaa.gov/). Wavelet software was provided by C. Torrence and G. Compo and is available at http://paos.colorado.edu/research/wavelets/. This is contribution 11366 from the Woods Hole Oceanographic Institution.

References

Anderson, S. P., K. Huang, N. J. Brink, M. F. Baumgartner, and R. A. Weller (2000), Pan American Climate Study data report, *Tech. Rep. 2000-03*, Woods Hole Oceanogr. Inst., Woods Hole, Mass.

Ballestero, D., and J. E. Coen (2004), Generation and propagation of anticyclonic rings in the Gulf of Papagayo, *Int. J. Remote Sens.*, *25*, 2217–2224.

Bendat, J. S., and A. G. Piersol (1971), *Random Data: Analysis and Measurement Procedures*, Wiley-Intersci., Hoboken, N. J.

Bendat, J. S., and A. G. Piersol (1986), *Random Data: Analysis and Measurement Procedures*, revised and expanded, Wiley-Intersci., Hoboken, N. J.

Bonjean, F., and G. S. E. Lagerloef (2002), Diagnostic model and analysis of the surface currents in the tropical Pacific Ocean, *J. Phys. Oceanogr.*, *32*, 2938–2954.

Chelton, D. B., R. A. DeSzoeke, M. G. Schlax, K. El Naggar, and N. Siwertz (1998), Geographical variability of the first baroclinic Rossby radius of deformation, *J. Phys. Oceanogr.*, *28*, 433–460.

Chelton, D. B., M. G. Schlax, J. M. Lyman, and G. C. Johnson (2003), Equatorially trapped Rossby waves in the presence of a meridionally sheared baroclinic flow in the Pacific Ocean, *Prog. Oceanogr.*, *56*, 323–380.

Chelton, D. B., M. G. Schlax, M. H. Freilich, and R. F. Millif (2004), Satellite measurements reveal persistent small-scale features in ocean winds, *Science*, *302*, 978–983.

Clarke, A. J. (1988), Inertial wind path and sea surface temperature patterns near the Gulf of Tehuantepec and Gulf of Papagayo, *J. Geophys. Res.*, *93*, 15,491–15,501.

Cronin, M. F., and M. J. McPhaden (1997), The upper ocean heat balance in the western equatorial Pacific warm pool during September–December 1992, *J. Geophys. Res.*, *102*, 8533–8553.

Enfield, D. B. (1987), The intraseasonal oscillation in eastern Pacific sea levels: How is it forced?, *J. Phys. Oceanogr.*, *17*, 1860–1876.

Fairall, C. W., E. F. Bradley, D. P. Rogers, J. B. Edson, and G. S. Young (1996), Bulk parameterization of air-sea fluxes during TOGA COARE, *J. Geophys. Res.*, *101*, 3747–3764.

Fofonoff, N. P. (1981), The Gulf Stream system, in *The Evolution of Physical Oceanography*, edited by B. A. Warren and C. Wunsch, pp. 112–139, MIT Press, Cambridge, Mass.

Giese, B. S., J. A. Carton, and L. J. Holl (1994), Sea level variability in the eastern tropical Pacific as observed by TOPEX and the Tropical Ocean-Global Atmosphere Tropical Atmosphere-Ocean Experiment, *J. Geophys. Res.*, *99*, 24,739–24,748.

Gill, A. E. (1982), *Atmosphere-Ocean Dynamics*, Elsevier, New York.

Gill, A. E., J. S. A. Green, and A. J. Simmons (1974), Energy partition in the large-scale ocean circulation of mid-ocean eddies, *Deep Sea Res.*, *21*, 499–528.

Gonzalez-Silvera, A., E. Santamaria-del Angel, R. Millán-Nuñez, and H. Manzo-Monroy (2004), Satellite observations of mesoscale eddies in the gulfs of Tehuantepec and Papagayo (eastern tropical Pacific), *Deep Sea Res., Part II*, *51*, 587–600.

Hansen, D. V., and G. A. Maul (1991), Anticyclonic current rings in the eastern tropical Pacific Ocean, *J. Geophys. Res.*, *96*, 6965–6979.

Hellerman, S., and M. Rosenstein (1983), Normal monthly wind stress over the world ocean with error estimates, *J. Phys. Oceanogr.*, *13*, 1093.

Hong, X., S. W. Chang, S. Raman, L. K. Shay, and R. Hodur (2000), The interaction between Hurricane Opal (1995) and a warm core ring in the Gulf of Mexico, *Mon. Weather Rev.*, *128*, 1347–1365.

Hosom, D. S., R. A. Weller, R. E. Payne, and K. E. Prada (1995), The IMET (Improved Meteorology) ship and buoy systems, *J. Atmos. Oceanic Technol.*, *12*, 527–540.

Jochum, M., and P. Malanotte-Rizzoli (2003), On the generation of North Brazil Current rings, *J. Mar. Res.*, *61*, 147–173.

Jochum, M., and R. Murtugudde (2004), Internal variability of the tropical Pacific Ocean, *Geophys. Res. Lett.*, *31*, L14309, doi:10.1029/2004GL020488.

Kaplan, J., and M. DeMaria (2003), Large-scale charcteristics of rapidly intensifying tropical cyclones in the North Atlantic basin, *Weather Forecast.*, *18*, 1093–1108.

Kessler, W. S. (1990), Observations of long Rossby waves in the northern tropical Pacific, *J. Geophys. Res.*, *95*, 5183–5217.

Kessler, W. S. (2002), Mean three-dimensional circulation in the northeast tropical Pacific, *J. Phys. Oceanogr.*, *32*, 2457–2470.

Kessler, W. S., M. J. McPhaden, and K. M. Weickmann (1995), Forcing of intraseasonal Kelvin waves in the equatorial Pacific, *J. Geophys. Res.*, *100*, 10,613–10,631.

Leeuwenburgh, O., and D. Stammer (2001), The effect of ocean currents on sea surface temperature anomalies, *J. Phys. Oceanogr.*, *31*, 2340–2358.

Levitus, S., and T. Boyer (1994), Temperature, in *World Ocean Atlas 1994*, vol. 4, *NOAA Atlas NESDIS 4*, U.S. Dep. of Commer., Washington, D. C.

Levitus, S., G. I. Monterey, and T. Boyer (1997), Seasonal variability of dynamic height and its fourier analysis, in *World Ocean Atlas 1994*, *NOAA NESDIS Atlas 15*, U.S. Govt. Print. Off., Washington, D. C.

Masina, S., S. G. H. Philander, and A. B. G. Bush (1999), An analysis of tropical instability waves in a numerical model of the Pacific Ocean, *J. Geophys. Res.*, *104*, 29,637–29,661.

Matsura, T., and T. Yamagata (1982), On the evolution of nonlinear planetery eddies larger than the radius of deformation, *J. Phys. Oceanogr.*, *12*, 440–456.

McCreary, J. P., H. S. Lee, and D. B. Enfield (1989), The response of the coastal ocean to strong offshore winds: With application to the Gulfs of Tehuantepec and Papagayo, *J. Mar. Res.*, *47*, 81–109.

McPhaden, M. J. (1996), Monthly period oscillations in the Pacific North Equatorial Countercurrent, *J. Geophys. Res.*, *101*, 6337–6359.

McWilliams, J. C., and G. R. Flierl (1979), On the evolution of isolated, nonlinear vortices, *J. Phys. Oceanogr.*, *9*, 1155–1182.

Miller, L., D. R. Watts, and M. Wimbush (1985), Oscillations of dynamic topography in the eastern Pacific, *J. Phys. Oceanogr.*, *15*, 1759–1770.

Molinari, J., D. Vollaro, S. Skubis, and M. Dickinson (2000), Origins and mechanisms of eastern Pacific tropical cyclogenesis: A case study, *Mon. Weather Rev.*, *128*, 125–139.

Montroy, D. L. (1997), Linear relationship of central and eastern North American precipitation to tropical Pacific sea surface temperature anomalies, *J. Clim.*, *10*, 541–558.

Moore, D. W., and S. G. H. Philander (1977), Modelling the tropical ocean circulation, in *The Sea*, edited by E. D. Goldberg et al., pp. 319–361, Wiley-Intersci., Hoboken, N. J.

Ostrom, W. M., B. S. Way, S. P. Anderson, B. Jones, E. Key, and G. Yuras (1999), Pan American Climate Study, Mooring Recovery Cruise Report, R/V *Melville*, cruise number PACS03MV, *Tech. Rep. 99-01*, Woods Hole Oceanogr. Inst., Woods Hole, Mass.

Pedlosky, J. (1987), *Geophysical Fluid Dynamics*, Springer, New York.

Pedlosky, J., and J. Thomson (2003), Baroclinic instability of time-dependent currents, *J. Fluid Mech.*, *490*, 189–215.

Perigaud, C. (1990), Sea level oscillations observed with Geosat along the two shear fronts of the North Equatorial Counter Current, *J. Geophys. Res.*, *95*, 7239–7248.

Philander, S. G. H. (1976), Instabilities of zonal equatorial currents, *J. Geophys. Res.*, *81*, 3725–3735.

Phillips, N. A. (1951), A simple three-dimensional model for the study of large-scale extra tropical flow patterns, *J. Meteorol.*, *8*, 381–394.

Raymond, D. J., et al. (2004), EPIC2001 and the coupled ocean-atmosphere system of the tropical east Pacific, *Bull. Am. Meteorol. Soc.*, *85*, 1341–1354.

Schlax, M. G., and D. B. Chelton (1994), Aliased tidal errors in TOPEX/POSEIDON sea surface height data, *J. Geophys. Res.*, *99*, 24,761–24,775.

Shay, L. K., G. J. Goni, and P. G. Black (2000), Effects of a warm oceanic feature on Hurricane Opal, *Mon. Weather Rev.*, *128*, 1366–1383.

Spillane, M. C., D. B. Enfield, and J. S. Allen (1987), Intraseasonal oscillations in sea level along the west coast of the Americas, *J. Phys. Oceanogr.*, *17*, 313–325.

Stern, M. E. (1975), Ocean circulation physics, *J. Fluid Mech.*, *428*, 349–386.

Stumpf, H. G., and R. V. Legeckis (1977), Satellite observations of mesoscale eddy dynamics in the eastern tropical Pacific Ocean, *J. Phys. Oceanogr.*, *7*, 648–658.

Thum, N., S. K. Esbensen, D. B. Chelton, and M. J. McPhaden (2002), Air-sea heat exchange across the northern equatorial sea surface temperature front in the eastern tropical Pacific, *J. Clim.*, *15*, 3361–3378.

Torrence, C., and G. P. Compo (1998), A practical guide to wavelet analysis, *Bull. Am. Meteorol. Soc.*, *79*, 61–78.

Trask, R. P., R. A. Weller, W. M. Ostrom, and B. S. Way (1998), Pan American Climate Study, Mooring Recovery and Deployment Cruise Report, R/V *Thomas Thompson*, cruise number 73, Tech. Rep. 98-18, Woods Hole Oceanogr. Inst., Woods Hole, Mass.

Umatani, S., and T. Yamagata (1991), Response of the eastern tropical Pacific to the meridional migration of the ITCZ: The generation of the Costa Rica Dome, *J. Phys. Oceanogr.*, *21*, 346–363.

Wang, W., and M. J. McPhaden (1999), The surface layer heat balance in the equatorial Pacific Ocean. part I: Mean seasonal cycle, *J. Phys. Oceanogr.*, *29*, 1812–1831.

Wang, W., and M. J. McPhaden (2001), The surface layer heat balance in the equatorial Pacific Ocean during the 1997–98 El Niño and 1998–99 La Niña, *J. Clim.*, *14*, 3393–3407.

Way, B. S., W. M. Ostrom, R. A. Weller, J. D. Ware, R. P. Trask, R. Cole, and J. Donovan (1998), Pan American Climate Study, Mooring Deployment Cruise Report, R/V *Roger Revelle*, cruise number Genesis 4, *Tech. Rep. 98-07*, Woods Hole Oceanogr. Inst., Woods Hole, Mass.

Weidman, P. D., D. L. Mickler, B. Dayyani, and G. H. Born (1999), Analysis of Legeckis eddies in the near-equatorial Pacific, *J. Geophys. Res.*, *104*, 7865–7888.

Weller, R. A., and S. P. Anderson (1996), Surface meteorology and air-sea fluxes in the western equatorial Pacific warm pool during the TOGA

Coupled Ocean-Atmosphere Response Experiment, *J. Clima.*, *9*, 1959–1990.

Weller, R. A., and R. E. Davis (1980), A vector measuring current meter, *Deep Sea Res., Part A*, *27*, 565–582.

Wunsch, C. (1997), The vertical partition of horizontal kinetic energy, *J. Phys. Oceanogr.*, *27*, 1770–1794.

Wunsch, C. (1998), The work done by the wind on the oceanic general circulation, *J. Phys. Oceanogr.*, *28*, 2332–2340.

Wyrtki, K. (1975), Fluctuations of the dynamic topography in the Pacific Ocean, *J. Phys. Oceanogr.*, *4*, 372–380.

Yamagata, T., K. Sakamoto, and M. Arai (1990), Locally-induced nonlinear modes and multiple equilibria in planetary fluids, *Pure Appl. Geophys.*, *133*, 733–748.

Zang, X., L. Fu, and C. Wunsch (2002), Observed reflectivity of the western boundary of the equatorial Pacific Ocean, *J. Geophys. Res.*, *107*(C10), 3150, doi:10.1029/2000JC000719.

Zhang, G. J., and M. J. McPhaden (1995), The relationship between sea surface temperature and latent heat flux in the equatorial Pacific, *J. Clim.*, *8*, 589–605.

Zhurbas, V., and I. S. Oh (2004), Drifter-derived maps of lateral diffusivity in the Pacific and Atlantic Oceans in relation to surface circulation patterns, *J. Geophys. Res.*, *109*, C05015, doi:10.1029/2003JC002241.

J. T. Farrar, MIT-WHOI Joint Program in Physical Oceanography, Mail Stop 29, Woods Hole Oceanographic Institution, Woods Hole, MA 02543, USA. (jfarrar@whoi.edu)

R. A. Weller, Department of Physical Oceanography, Woods Hole Oceanographic Institution, Clark 204A MS 29, Woods Hole, MA 02543-1052, USA.